INVESTIGATION OF IMPEDANCE-MATCHING TECHNIQUES FOR INFRARED ANTENNAS

by

Camilo A. Moreno Cleves

A dissertation submitted to the faculty of
The University of North Carolina at Charlotte
in partial fulfillment of the requirements
for the degree of Doctor of Philosophy in
Optical Science and Engineering

Charlotte

2020

Approved by:

_____
Dr. Glenn Boreman

_____
Dr. Tino Hofmann

_____
Dr. Vasily Astratov

_____
Dr. Kathryn Smith

ABSTRACT

CAMILO A. MORENO CLEVES. Investigation of impedance-matching techniques for infrared antennas. (Under the direction of DR. GLENN BOREMAN)

In this study, we used scattering-scanning near-field optical microscopy (s-SNOM) to experimentally characterize several structures relevant to infrared (IR) antenna technology, by measuring the electric near-field strength as a function of position on metallic antennas and transmission lines. Having spatially resolved measurements of electric field amplitude allows assessment of the wave impedance at any location on a standing-wave structure. We improved the usual s-SNOM data-processing method using a principal-components decomposition to allow unambiguous phase retrieval. We demonstrated the efficacy of this technique on IR bow-tie antennas of continuous and discrete designs, allowing comparison of their polarization dependence and spatial response distribution. This phase-retrieval procedure was used throughout our investigations. An IR sensor of particular interest is the antenna-coupled metal-oxide-metal (MOM) diode, which rectifies IR-frequency current waves collected by the antenna to produce an output voltage proportional to the incident irradiance. These sensors are appealing because they have a fast response and do not require cryogenic cooling. IR antennas have a typical impedance in the range of tens of Ohms at resonance, while MOM diodes have impedance in the range of thousands of Ohms. This impedance mismatch is a limiting factor in the detection sensitivity that can be achieved with antenna-coupled MOM diodes. To address this issue, we studied two impedance-matching techniques. The first is based on the fact that a MOM diode under DC bias exhibits a change in its dynamic resistance. We obtained measurements that demonstrate modification of IR-frequency current waves using diodes contained in the antenna structure. The ability to tune the operating point of a MOM diode and thereby modify antenna or transmission-line impedance at IR

frequencies offers the possibility of active impedance-matching networks. The second technique we investigated involved tailoring of the feed-point geometry to obtain an antenna with higher impedance that offers better matching. We designed, fabricated and demonstrated several new IR-antenna designs that have impedance in the range of 1000 Ohms. This new class of antennas stands to improve signal-transfer efficiency to high-impedance IR sensors such as MOM diodes.

DEDICATION

To Sandra, Camilo and Sergio.

ACKNOWLEDGEMENTS

The work in this dissertation was possible with the support of many people which I want to thank. First, I thank Dr. Glenn Boreman for giving me the opportunity to participate in fascinating projects under his direction and advisory. His constant encouragement and support along these projects offered me the opportunity to learn, challenge myself and grow as a scientist, as a professional and as a person.

I thank Dr. Javier Alda at the Universidad Complutense de Madrid, Dr. Ed Kinzel at the University of Notre Dame and Earl Ritchie at the University of North Carolina at Chapel Hill for teaching the background and operation of the scattering-scanning near-field optical microscope, key instrument that made possible the experiments on this dissertation, and for their continuous support over the years. Additionally, I thank Dr. Robert Parks for his assistance that time when the CO_2 laser failed and helping me bringing the s-SNOM back to work.

I thank Scott Williams, Mike Dhooghe, Dr. Lou Deguzman, Dr. Jeffery Thousand, Dr. Jeffrey D' Archangel, Dr. Eric Tucker and Dr. Daniel Fullager for teaching me the antenna microfabrication, for all their assistance and patience through the process and availability for troubleshooting experimental problems. I thank Dr. Brian Lail, and his student Edriss Mirnia at Florida Institute of Technology; as well as Dr. Tino Hofmann and his students Serang Park and Yanzeng Li for their guidance with COMSOL.

I thank Dr. Javier Gonzalez and his group at the Universidad Autónoma de San Luis Potosí for offering the collaboration to study the discrete bow-tie antennas, as well as Dr. James Ginn at Plasmonics Inc. for the collaboration and insightful discussions when studying antenna-coupled diodes.

I thank my cohort friends Ossama Tfeily, Joel Solomon, Joseph Mays, Rahma Nawab, Dr. Patrick Thewlis, Sajjad Hossain, Sara Moein, Dr. Jack Chang, Dr. Yuanye Liu, Dr. Navid Farahi and Carlos Rodriguez for their friendship and support

during my time in graduate school while I am far away from home. Additionally, I thank my friends from the online community The Grad Swamp, that despite the distance and the different time zones they offered me kind support, valuable academic advice, and encouragement throughout graduate school.

I thank the Center of Optoelectronics and Optical Communications at the University of North Carolina at Charlotte and the Graduate School for support for my research.

Last but not least, I thank my parents, Sandra and Camilo, and my brother Sergio for believing in me since the very beginning, for supporting me through all these years and for being with me during every step of my academic and professional journey.

TABLE OF CONTENTS

LIST OF TABLES

LIST OF FIGURES

LIST OF ABBREVIATIONS

AFM Atomic force microscope

AUT Antenna under test

BS   Beam splitter

CPS Coplanar strip line

EBL Electron-beam lithography

EBPVD Electron-beam physical vapor deposition

EM Electromagnetic

FEM Finite element method

IPA Isopropyl alcohol

LIA Lock-in amplifier

MCT Mercury cadmium telluride

MFD Modified folded dipole

MIBK Methyl isobutyl ketone

MOM Metal-oxide-metal

OAP Off-axis parabolic

PMMA Polymethyl methacrylate

RF   Radio frequencies

s-SNOM Scattering-type scanning near-field optical microscopy

SNR Signal-to-noise ratio

CHAPTER 1: INTRODUCTION

The infrared interval of the electromagnetic (EM) spectrum corresponds to radiation with wavelengths longer than the visible and shorter than millimeter, this is from 0.8 μm for the near infrared to the submillimeter region (100 μm - 1 mm). The formal study of infrared radiation dates to 1800 when the astronomer Sir William Hershel first observed the evidence its existence. As he passed a sunlight beam through a prism and placed a thermometer beyond the red portion of the refracted beam, the thermometer registered a temperature change [1]. After this, infrared radiation was measured by exploiting the thermal changes on matter that cause changes in other physical properties that can be quantified. This phenomena gives rise to thermal based detectors such as thermopiles (in which temperature changes produces a voltage due to thermoelectric effect), bolometers (electrical resistance changes are produced), and Golay cells (pressure changes on a gas is produced). Thermal based detectors are easily adaptable to suit different types of applications, however their response time is limited to how quick the material reacts to temperature changes [2].

With the advent of the twentieth century, novel developments in semiconductor and material science proved that infrared detectors can be optimized. The implementation of photoconductive compounds such as lead sulfide created practical applications for infrared sensors due to the efficient absorption of photons particularly with a wavelength of 3 μm [3]. Additionally, detectors based on narrow band semiconductors offered extensive wavelength sensing capabilities with improved sensibility. Specifically, alloys such as mercury cadmium telluride (HgCdTe or MCT) allowed the tailoring of the bandgap and, as a consequence, the frequency response of the sensor to better fit the application while having high absorption, high electron mobility

and low thermal generation. These type of detectors are known as photon detectors. However, optimal performance of these detectors require operation at temperatures as low as 77 K. This limitation restricts the application environments for such detectors.

Because of limited response time or low temperature requirements, alternative methods to construct infrared detectors are necessary. One method that has been proven to address these limitations is the coupling of the infrared detector to an antenna operating in the infrared [4, 5].

1.1   Infrared Antennas

Antennas are devices that convert free electromagnetic waves into guided waves and vice versa [6]. They have been a key component in radio and microwave wireless communications in the past decades. Typically, the characteristic dimension of an antenna is similar to the wavelength of operation, e.g. in the order of meters for radio and microwaves, but smaller for higher frequencies. By exploiting this simple property an antenna can be used as a device that is sensitive to a certain range of wavelengths and polarization which depends on the design chosen. Antennas for the radio frequencies (RF) and microwaves are well understood, and a wide variety of designs offer solutions for satellite communications systems, radar systems, remote sensing and medical diagnosis [7].

Studies of antennas in the IR or visible range were not explored until the development of nanofabrication technologies, such as focused ion-beam milling and electron-beam lithography. These techniques made the fabrication of antennas on the nanoscale feasible, enabling integration of antennas into nano applications [8]. Since then, infrared antennas have been applied with advanced accuracy and time response in thermography, imaging, chemical compound detecting and polarization detection [9].

By exploiting the field-coupling properties that antennas have, these can be implemented in conjunction with infrared detectors to obtain an efficient method to

deliver energy, from incident radiation, in the form of a voltage [10] and improve the sensitivity and multispectral polarization response of the detector [11]. It has been demonstrated that the implementation of antenna-detector coupling enhances photogeneration of carriers in semiconductor materials, improving generation of the photocurrent in photodiodes [12]. This concept has been applied to half-wave dipole antennas coupled to a photodiode, which demonstrated enhancement of the device sensitivity [13]. With this type of coupling, improvements in the signal-to-noise ratio (SNR) for infrared detectors has been achieved. In these devices, an antenna is coupled to a metal-oxide-metal (MOM) diode and different fabrication parameters for the diode can tune the resistance [14]. Furthermore, this approach can be extended to the design of photovoltaic devices, in which plasmonic antennas enhance the incident fields thus improving the performance of the solar cell [15]. While optical antennas can improve the performance of photodetectors, photovoltaic devices, and enhance imaging applications in the nanoscale [16] and IR frequencies, new challenges in infrared antennas arise. One such challenge is antenna-diode impedance mismatch.

1.2   Antenna Impedance

Antennas are characterized by their input impedance, defined as the ratio between the voltage V and current I at the terminals of the antenna. In general, the impedance is a complex quantity defined as

$$Z = \frac{V}{I} = R + iX, \tag{1.1}$$

where the resistance R is given by the radiation resistance and loss resistance $R = R_r + R_L$, and the reactance X. To study the efficiency of an antenna, let an EM wave be incident into an antenna with impedance $Z_A = R_A + iX_A$. The antenna is connected to a load with impedance $Z_L = R_L + iX_L$. The power P_r delivered from

the antenna to the load can be expressed by

$$P = \frac{1}{2}|I_L|^2 R_A = \frac{|V_L|^2}{2}\left[\frac{R_L}{(R_A + R_L)^2 + (X_A + X_L)^2}\right]. \tag{1.2}$$

The power delivered is maximum when $R_r + R_L = R_L$ and $X_A = -X_L$. This implies that the most efficient power transmission from the antenna to the load occurs when the impedances are in conjugate match, i.e. $Z_A = Z_L^*$. For this reason it is important to determine the impedance of both the antenna and the elements this antenna is connected to and attempt to match them as closely as possible.

The direct measurement of the antenna impedance is performed by considering the antenna connected to a transmission line, which is usually the case in practical applications. The degree of mismatch between these elements determines the amount of power reflected at the input of the antenna terminals into the line compared to the incident power [17]. The degree of mismatch depends on the antenna input impedance Z_A, the characteristic impedance of the transmission line Z_{cps}, and the reflection coefficient by the relationship

$$\frac{P_{\mathrm{ref}}}{P_{\mathrm{inc}}} = |\Gamma|^2 = \frac{|Z_A - Z_{\mathrm{cps}}|^2}{|Z_A + Z_{\mathrm{cps}}|^2}, \tag{1.3}$$

where P_{ref} is the reflected power, P_{inc} is the incident power and Γ is the reflection coefficient at the antenna input terminals. Experimentally, it is common to compute Γ. If the impedance of the transmission line is known, the antenna impedance is given by

$$Z_A = \frac{1 + \Gamma}{1 - \Gamma} Z_{\mathrm{cps}}. \tag{1.4}$$

The typical impedance of the dipole antenna is 75Ω (at resonance, i.e. Im$\{Z\} = 0$)

[18]. While for a MOM diode the resistance is given by

$$R_D = \frac{\sigma}{\pi A} + \frac{\rho}{2\sqrt{A}}, \tag{1.5}$$

where A is the diode contact area, σ and ρ are the resistivities of the oxide film and metal, respectively [19]. R_D is typically on the order of 1-10 kΩ or above. Hence the power transmission between the antenna and load is diminished due to the impedance mismatch among these elements. Therefore the study of impedance matching techniques in this scale is of major interest for IR and optical antennas.

Recent investigations on impedance tuning for optical antennas include numerical studies of a nanodipole with nanoparticles [20], a Hertzian nanoantenna with nanoloads [21], and impedance tuning on a receiving and emitting antenna with varying dimensions to obtain impedance matching [22]. Additionally, experimental reports show that illuminating nanorods with bridges can tune antenna impedance [23]. Experimental measurement of input impedance of a folded dipole nanoantenna has recently been achieved using scattering-type scanning near-field optical microscopy (s-SNOM) [24]. However, experimental implementation of impedance matching techniques design in IR antennas has not been attempted. To address this challenge, we investigate the capabilities of two matching networks whose purpose is to increase the impedance of the microstrip dipole antenna, so the mismatch with respect to the impedance of a typical diode is reduced. These investigations are discussed in Chapter 5.

CHAPTER 2: FUNDAMENTALS OF MICROSTRIP ANTENNA DESIGN AND FABRICATION

The design procedure involves the optimization of the antenna dimensions, geometry and components so the antenna has a high impedance that could match the impedance of a diode. For this, a full-wave electromagnatic field simulator can be used to evaluate the performance of the antennas and fine tune a design to achieve good performance while the antenna fabrication remains feasible. This chapter describes the general procedure for designing the antennas studied in this thesis.

2.1   Effective wavelength

One of the fundamental antennas is the dipole, which consists of a cylinder of conductive and lossless material with a gap in the middle for the feed. One of the most common dipole designs in the RF is is the half-wavelength dipole, whose length L is equal to half of the wavelength $\lambda/2$ of the incident EM wave. This choice allows the antenna to be resonant, i.e. a standing wave of current is created in the conductor. However when considering more complex antenna types, this choice for antenna length changes. This is the case of microstrip antennas, which consist of a metallic strip, thinner than the free-space wavelength, placed a small fraction of a wavelength above a ground plane. The strip and ground plane are separated by a dielectric sheet, also known as substrate or stand-off layer. In this open geometry, electric fields are partially in the dielectric which gives rise to a phenomena known as fringing. The amount of fringing depends on the dimensions of the strip, the thickness of the substrate and its dielectric constant. Because of fringing the, the electrical width of the strip is larger compared to its physical dimensions. This shift

impacts the performance of the antenna, therefore it has to be taken into account in the design process [17].

When transferring this design from the RF to optical frequencies, common metals do not exhibit perfect reflection of incident waves at their surface, and because of the skin effect oscillations of the free electrons appear. As a result, a half-wavelength dipole is not resonant for an incident wave of a given wavelength, it will be resonant for a shorter effective wavelength λ_{eff} [25]. For an EM wave with wavelength λ, the effective wavelength is

$$\lambda_{\text{eff}} = 2\pi R \left(a_1 + a_2 \frac{\lambda}{\lambda_p} \right) - 4R, \tag{2.1}$$

where R is the antenna arm radius, λ_p is the plasma wavelength and a_1, a_2 are constants. In the case of electromagnetic waves from a CO_2 laser ($\lambda = 10.6~\mu$m) incident into an antenna 150 nm thick and made of gold located at the interface of a zinc sulfide (ZnS) substrate and air, Eq. (2.1) predicts the antenna length should be $L = \lambda_{\text{eff}}/2 = 3.6\mu$m for the antenna to be resonant. This length is a indication of the antenna length to seek in the design procedure. Numerical simulations that implement the finite-element method can be used to verify or correct this prediction.

2.2   Design with Finite-Element Method

For simple antennas the assumptions from Eq. 2.1 can be accurate, but when the geometry of the antenna gets more complex, these predictions are not longer accurate. However, it offers a guidance as starting point for the design process. For more accurate modeling, the antenna-wave interaction has to be considered as a full electrodynamic problem. This interaction is governed by Maxwell's equations, which for harmonically varying fields with angular frequency $\omega = 2\pi f$, are given by

$$\nabla \times \mathbf{E} = -i\omega\mu\mathbf{H} - \mathbf{M} \tag{2.2}$$

$$\nabla \times \mathbf{H} = i\omega\varepsilon\mathbf{E} + \mathbf{J} \tag{2.3}$$

$$\nabla \cdot (\varepsilon \mathbf{E}) \;=\; \rho \tag{2.4}$$

$$\nabla \cdot (\mu \mathbf{H}) \;=\; \rho_m, \tag{2.5}$$

where $\mathbf{E}$ and $\mathbf{H}$ are the electric and magnetic field respectively, $\mathbf{J}$ and $\mathbf{M}$ are the electric and magnetic current densities, respectively, ρ and ρ_m are the electric and magnetic charge densities, respectively. The materials in which the fields propagate are characterized by $\varepsilon = \varepsilon_0 \varepsilon_r$ with $\varepsilon_0 = 8.85 \times 10^{12}$ F/m as the free space permittivity and ε_r is the medium's relative permittivity, and $\mu = \mu_0 \mu_r$ with $\mu_0 = 4\pi \times 10^{-7}$ H/m as the free space permeability and μ_r is the medium's relative permeability.

After combining the Faraday's and Ampère-Maxwell's Laws (Eqs. (2.2) and (2.3)), assuming homogeneous media and no sources, it is found that the electric fields satisfy the wave equation

$$\nabla^2 \mathbf{E} + k^2 \mathbf{E} = 0, \tag{2.6}$$

and considering the three components of the vector field, each component satisfies the Helmholtz equation.

Depending on the complexity of the problem, the wave equation might or might not have analytic solutions. When there is no analytical solution, numerical methods can be used to find approximations to such solutions. One method that is widely used is the Finite Element Method (FEM) [26]. Briefly, in FEM the domain of the problem is discretized into N nodes generating $N-1$ intervals (or elements) small enough, typically $\lambda/10$, so that the solution of the fields at the nodes can be approximated by an expansion of linear functions. The coefficients in this expansion become the unknowns, and by introducing boundary conditions, the differential equation can be written as a system of N equations with N unknowns that can be expressed in matrix form as

$$A\mathbf{u} = \mathbf{b}, \tag{2.7}$$

where A is a $N \times N$ matrix whose elements are related to the media properties and fields frequency, $\mathbf{u}$ is a $N \times 1$ vector whose components represent the field at each node and $\mathbf{b}$ is a $N \times 1$ vector that accounts for the boundary conditions and sources. Solutions for the fields in Eq. (2.7) can be found by using direct solvers such as the lower-upper (LU) decomposition method to obtain numerical insight of the electric field in the domain of the problem.

Commercial software such as COMSOL offers a straightforward solution to implement the FEM. Its graphical user interface allows a straightforward construction of the geometry and components of an antenna in the 3D space along with the definitions of the material properties, the excitation and boundary conditions. COMSOL then splits the domain into the elements of the FEM to solve for the fields in the simulation domain. Additionally, this software allows the user to apply different excitation conditions, boundary conditions and parametric sweeps to obtain insights into the model. For this reason COMSOL was employed in this dissertation to model the behavior of the antennas proposed and, based on numerical results, select the designs of the antennas to be fabricated.

2.3   Ellipsometry

To obtain accurate predictions from the antenna simulations, the input parameters in the models need to be nominally the same as the real antenna. Hence, the materials specified in COMSOL should be realistic, i.e., the optical properties such as permittivity and conductivity of the media in the model should be equal to the properties of real materials at IR frequencies. Infrared ellipsometry can be used to measure the optical properties of such materials. Ellipsometry is an experimental technique to measure the refractive index n and extinction coefficient κ of a thin layer of a metal or dielectric. In this technique, a beam with the frequency of interest is incident into the thin film under test and a set of polarizers are used to measure the p-pol and s-pol components of the reflected beam from the thin film. With these
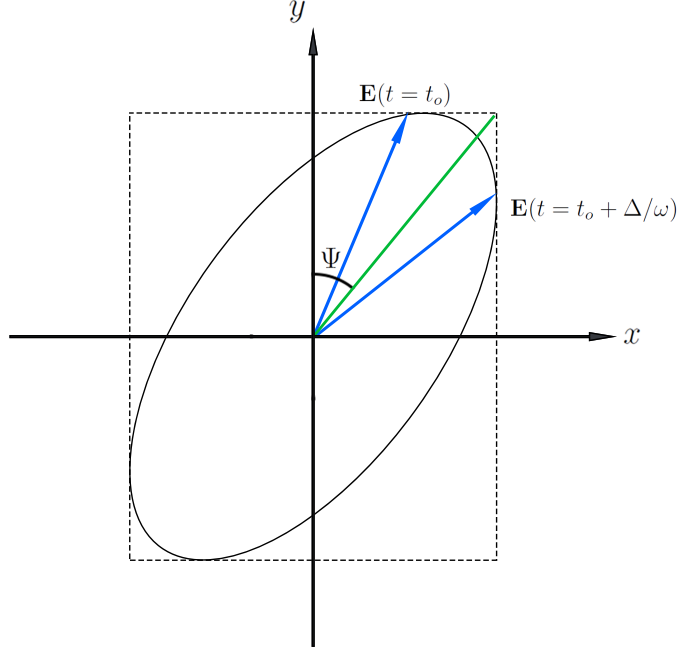
Figure 2.1: Ellipsometric angles Ψ and Δ that arise from the elliptic nature of the polarization of EM waves. Blue arrows depict the electric field at an instant t_o and $t_o + \Delta/\omega$.

two components, the two ellipsometric angles shown in Fig. 2.1 can be determined: Ψ, which is related to the relative amplitude of the field components and Δ, which is related to the relative phase between the components [27]. Then, the reflectivity can be written as

$$\rho = \tan \Psi e^{i\Delta}. \tag{2.8}$$

This expression should be consistent with the Fresnel equations for reflection, so a model for the approximation of the complex refractive index $\tilde{n} = n + i\kappa$ of the thin film can be applied and then it is fitted to experimental measurements. From this, the relative permittivity ε_r and conductivity σ can be calculated as [28]

$$\varepsilon_r = \varepsilon_1 + i\varepsilon_2, \tag{2.9}$$

$$\varepsilon_1 = n^2 - \kappa^2, \tag{2.10}$$

$$\varepsilon_2 = 2n\kappa, \tag{2.11}$$

$$\sigma \;\; = \;\; 2\varepsilon_0 n\kappa\omega. \tag{2.12}$$

Once the optical properties of the media are determined, these can be used in COM-SOL to simulate the propagation of the fields more accurately. In this dissertation, we have measured the optical properties of metals and dielectric thin films using the IR ellipsometer manufactured by J.A. Wollam Co. This instrument allows the measurement of n and κ over the spectral range from 2 μm to 45 μm.

2.4   Antenna Fabrication

The antennas and resonant structures studied in this dissertation were fabricated using electron-beam lithography and thin film deposition, techniques that are briefly described in this section.

2.4.1   Electron-beam Lithography

Due to the small dimensions of the antennas, electron beam lithography (EBL) is used for antenna the fabrication. In essence, EBL consists of an electron beam incident on a sample coated with resist that is sensitive to the electrons [29]. An EBL system is composed of an electron source, an electron column and a mechanical stage. The fabrication of the antennas was performed using the Raith 150 e-beam tool, which has a thermal field-emission electron source [30]. In this type of source, a sharp tungsten needle is heated to 1800 K, exciting electrons so they overcome the work function barrier and are extracted from the material. Once the electrons are free, a set of magnets accelerate, shape and focus the electron beam to a 5 nm spot on the sample. The electrons penetrate the resist in the sample and experience small angle scattering (forward scattering) causing broadening of the beam diameter. As the electrons penetrate into the substrate, they experience large angle scattering (backscattering), causing proximity effects. Backscattered electrons continuously slow down as they travel, producing the so-called secondary electrons, a cascade of low energy electrons.

The bulk of the resist exposure process is due to secondary electrons. A resist can be either positive or negative. When a positive resist is exposed, its molecular structure changes and bonds get broken, making the exposed resist soluble to a developer. In contrast, a negative resist is polymerized when exposed making it difficult to dissolve. As a result, areas in a positive resist that were exposed will be washed away in the developing process, producing a positive image of the pattern. Areas in a negative resist that were exposed will remain on the surface when developed washing away the non-exposed areas, producing in this way a negative image. In this dissertation, the fabrication of the antennas used polymethyl methacrylate (Micro-chem 950 PMMA A4) as a positive e-beam resist. The developer used was a solution of methyl isobutyl ketone (MIBK) and isopropyl alcohol (IPA).

2.4.2   Metallization

Another technique used in antenna fabrication is metallization. This process involves growing a thin layer of metal above the substrate from which to fabricate the antennas. Electron-beam physical vapor deposition (EBPVD) is a reliable technique for metallization. In EBPVD, a electron beam is thermally generated in a similar fashion as described in the previous section. An electric field then accelerates the electrons to a high kinetic energy and a magnetic field guides the beam towards a crucible containing the material to be evaporated [31]. Upon collision, the kinetic energy of the electrons is converted into various forms of energy due to the interaction of the electrons with the atoms of the evaporating material as the electrons strike its surface. The thermal energy from this interaction is utilized to melt or sublimate the material to produce the desired vapor pressure. Under high vacuum conditions (10^{-6} Torr), evaporated molecules are less likely to lose kinetic energy so they can be deposited on the sample and the thin layer starts to grow. When the desired thickness is achieved, the e-beam flow can be stopped to end the evaporation process. The Kurt J. Lesker PVD 75 thin film deposition system with e-beam source was used

for the fabrication of the antennas studied in this dissertation.

CHAPTER 3: ANTENNA TESTING

In Chapter 1 it was established the importance of having impedance matching in an antenna-coupled detector and the possibility to quantify such impedances. However, the dimensions for infrared antennas, typically in the order of micrometers or nanometers, make the measurement of impedance a challenge. A proven method to measure the impedance of a microstrip antenna involves the sampling of the near field along the antenna using scattering-type scanning near-field microscopy (s-SNOM) [24].

In microscopy the limit of an imaging system is given by Abbe's resolution limit, which establishes that, due to diffraction, the smallest resolvable distance d between two points to image depends on the wavelength λ and the numerical aperture (NA) of the system ($d = \lambda/2NA$). But s-SNOM breaks this limit and can achieve resolution beyond this by several orders of magnitude [32]. This improvement in resolution is achieved by the implementation of a metallic probe with a sharply tipped end, which enhances an external optical field applied upon it. In s-SNOM the tip intercepts and radiates incoming light in a similar fashion as an antenna, and provide an optical field to probe the optical response of a sample. Proper modulation of the separation between tip and sample allows observation of localized field scattering. Because of this, the resolution of the system is limited by the probe's tip size.

The interaction between the tip and the sample can be modeled from electrostatic theory [33]. The tip can be approximated as a polarizable sphere of radius a and polarizability α, and the sample underneath is considered either a dielectric or a metal with a permeability ϵ. If the tip is above the sample at a distance z and an external electric field E is applied, then the sphere is polarized with dipole moment

$p = \alpha E$, so the electric field of the induced dipole given by

$$E_{\text{dipole}}(r) = \frac{p}{2\pi r^3}. \tag{3.1}$$

This electric field induces surface charges in the sample. The resultant fields can be described by an image dipole inside the sample, with a dipole moment $p' = \beta p$, where $\beta = (\epsilon - 1)/(\epsilon + 1)$. Then, the incident field at the probe gets enhanced by the image field, modifying the probe dipole moment which can be rewritten as

$$p = \frac{\alpha}{1 - \dfrac{\alpha\beta}{16\pi(z+a)^3}} E. \tag{3.2}$$

The probe-sample system generates a total field given by the superposition of the probe and image dipole fields, with an effective polarizability for the system given by

$$\alpha_{\text{eff}} = \frac{\alpha(1+\beta)}{1 - \dfrac{\alpha\beta}{16\pi(z+a)^3}}. \tag{3.3}$$

So the scattered far field $E_{\text{sca}} = \alpha_{\text{eff}} E$ is strongly enhanced at short distances $z < a$ and most importantly it measures both the amplitude and phase of the complex near-field interaction. Therefore, s-SNOM is a tool that allows retrieval of the near-field interaction with high resolution beyond the diffraction limit.

3.1   s-SNOM

From the experimental point of view, the operational principle of the s-SNOM is based on a Michelson interferometer. As shown in Fig. 3.1, an incident collimated beam from a CO_2 laser (Access Laser, model L4SL) operating at $\lambda = 10.6$ μm (28.3 THz) and linearly polarized, is both transmitted and reflected by a zinc selenide (ZnSe) beam splitter (BS). The transmitted beam serves as the reference beam while the reflected beam is the test beam. The reference beam propagates to the reference

mirror which is mounted on a piezostage (Physics Instruments, model E-665) that allows it to oscillate axially at a frequency $f_{mirror} = 300$ Hz and amplitude $\Delta L = 2.2$ μm. Because of this feature it is said that s-SNOM operates in pseudo-heterodyne mode of detection.
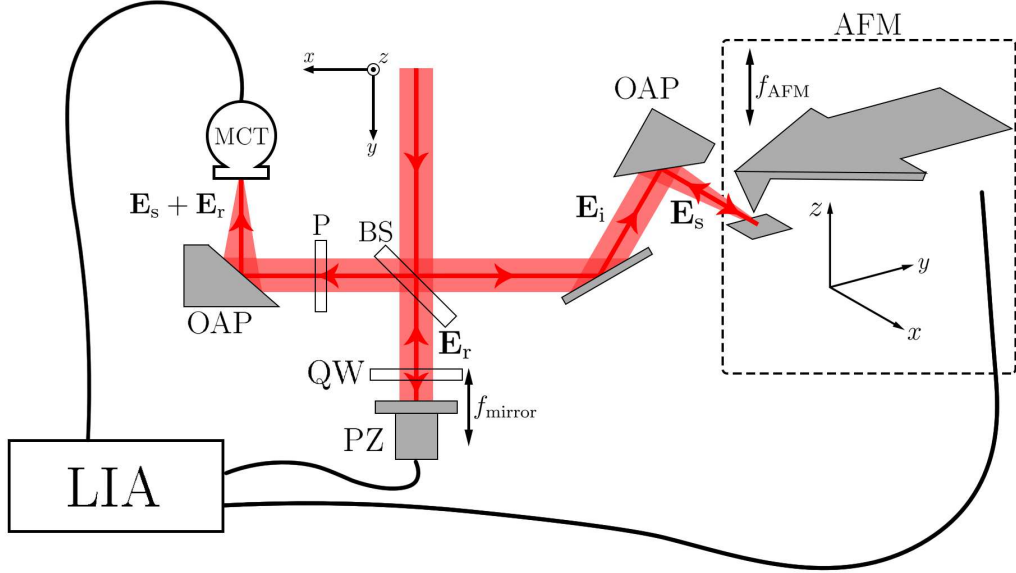
Figure 3.1: Schematic s-SNOM setup

The beam reflected from the BS is focused by an off-axis parabolic (OAP) mirror into the antenna under test (AUT) at a 60° incidence angle. The AUT is in the xy plane and placed under an atomic force microscope (AFM, Veeco/Bruker Innova, model 1A325) operating in tapping mode so its Si (platinum coated) cantilever tip (NanoWorld Arrow-NCPt-20) oscillates along the z plane at a frequency $f_{AFM} =$ 250-270 kHz. The propagation direction of incident beam is contained in the yz plane and the electric field is s-polarized along the x-axis so that it interacts with the AUT. This leads to near-field interaction between tip and sample, which scatters predominantly the E_z component of the near field. The scattered near field is reflected by same OAP mirror back to the BS. The reference and scattered fields are added and another OAP focuses them into a liquid-nitrogen-cooled mercury cadmium telluride (MCT) detector. A wire grid polarizer is used to suppress background scattering

coming from the tip shaft. As the AFM tip explores the AUT, the sample holder moves in a raster scan in the xy plane in order to obtain a two-dimensional map of the near-field distribution along the antenna. The signal registered by the MCT detector is acquired by a lock-in amplifier (LIA) synchronized with the AFM. The purpose of this method is explained in the next subsection.

3.1.1   Lock-in amplifier

When the AFM operates in tapping mode, the tip vibrates at a frequency f_{AFM} and if the amplitude of this oscillation is $A \ll \lambda$, then the near-field interaction generates light scattering at higher harmonics with frequency $f_n = nf_{\text{AFM}}$ with n an integer [33]. The background noise is confined to the dc and lower harmonics, and is smaller for higher harmonics. The LIA is used to register the signal at those higher harmonics. The way the LIA acquires a signal at a certain frequency is by the demodulation technique. Let V_s be the test signal with amplitude R and frequency ω_s, and let V_r be the reference signal with frequency ω_r described as

$$V_s(t) = \sqrt{2}R\cos(\omega_s t + \theta) = \frac{R}{\sqrt{2}}\left(e^{i(\omega_s t + \theta)} + e^{-i(\omega_s t + \theta)}\right), \tag{3.4}$$

$$V_r(t) = \sqrt{2}e^{-i\omega_r t} = \sqrt{2}(\cos\omega_r t - i\sin\omega t). \tag{3.5}$$

The demodulation involves mixing these two signals and taking the temporal average. Mathematically the mixing implies the product between these two signals, so the mixed signal $Z(t)$ is

$$Z(t) = V_s(t)V_r(t) = R\left[e^{i((\omega_s - \omega_r)t + \theta)} + e^{-i((\omega_s + \omega_r)t + \theta)}\right] \tag{3.6}$$

$$= X(t) + iY(t). \tag{3.7}$$

The mixed signal can be averaged over a period of time, so the output is $\langle Z(t)\rangle$. When the period is long enough, the high-frequency component can be filtered out,

i.e. $\langle e^{-i((\omega_s+\omega_r)t+\theta)}\rangle = 0$. So the output signal reduces to

$$\langle Z(t)\rangle = R\langle e^{i((\omega_s-\omega_r)t+\theta)}\rangle = Re^{i\theta} \tag{3.8}$$

for $\omega_s = \omega_s$ and it is zero for $\omega_s \neq \omega_s$. This way the LIA returns the amplitude of the signal in terms of $X = R\cos\theta$ (called the in-phase component) and $Y = R\sin\theta$ (called the quadrature component) of a signal with the same frequency as the reference signal. Therefore if the frequency of the reference signal is an integer multiple of f_{AFM} (i.e. a harmonic), then the LIA returns the amplitude and phase of the test signal demodulated at this harmonic. The amplitude R and phase θ of this signal are given by

$$R = \sqrt{X^2 + Y^2}, \qquad \theta = \arctan(Y/X). \tag{3.9}$$

The phase θ in Eq. (3.9) is the phase of the harmonic signal with respect to the reference signal. However, to measure the phase of the near-field, interferometry techniques have to be implemented.

3.1.2 Pseudoheterodyne scheme

Despite that the scattering background originating from the tip shaft of the AFM is suppressed at higher harmonics, it has been shown that it is not completely eliminated, leading to artifacts in the near-field measurements [34]. However pure near-field recovery is achieved by introducing a sinusoidal phase modulation on the reference mirror on the reference arm of the interferometer. This technique of phase modulation on the reference wave is referred as *pseudoheterodyne* mode. In this scheme, the phase of the reference beam is modulated by oscillation of the reference mirror at a frequency f_M such that $f_M \ll f_{\text{AFM}}$, and with an amplitude $\Delta l = \gamma\frac{\lambda}{4\pi}$, where it is advantageous to have a modulation depth $\gamma = 2.63$ (this choice of γ simplify the field computation, details on the derivation of γ are shown in Appendix A). This modulation generates sidebands around the harmonics of the cantilever vi-

bration. So the nth scattered harmonic with frequency nf_{AFM} splits into sidebands with frequencies $f_{n,m} = nf_{AFM} + mf_M$, where n and m are integers. To detect this signal, the LIA is configured to measure the demodulated signals from the detector at the first and second sidebands ($m = 1, 2$) of the second harmonic of the cantilever frequency ($n = 2$), designated as $S_{2,1}$ and $S_{2,2}$. As demonstrated in [35], the complex amplitude of the near-field E_z component is given by

$$E_z(x, y) = \kappa \left[S_{2,2}(x, y) - iS_{2,1}(x, y) \right] \exp(i\Psi_G), \tag{3.10}$$

where κ is a real number that accounts for the detector response, the transmissivity of the s-SNOM optical system, and the reference beam amplitude; and Ψ_G is the global phase factor. Thus, the modulus and phase of the near-field component $E_z(x, y)$ are given by

$$|E_z(x, y)| = \kappa \sqrt{S_{2,2}^2(x, y) + S_{2,1}^2(x, y)}, \tag{3.11}$$

$$\phi(x, y) = \Psi_G - \Phi(x, y), \tag{3.12}$$

$$\text{where } \Phi(x, y) = \arctan[S_{2,1}/S_{2,2}]. \tag{3.13}$$

Experimental limitations arise since the measurements of the signals $S_{n,m}$ obtained from the LIA correspond to the modulus of the locked signal, i.e., they are always positive valued. Meaning, from Eq. (3.13), the actual phase could be one of four possible angles: Φ, $\pi - \Phi$, $\pi + \Phi$ or $2\pi - \Phi$. Therefore we developed a technique that allows the correct measurement of the phase.

3.1.3 Phase Retrieval

To overcome the ambiguity of the phase, the LIA is set to record the X and Y components of the locked signal, components that can be either positive or negative. This way, the collected signals from the sidebands $S_{n,m}$ have a sign, so when calculat-

ing the phase using Eq. (3.13), the arctan function will return a unique angular value within the $[0, 2\pi)$ range. The whole range can be accessed by using the two-argument version of the arctan function, typically denoted as atan2(Y, X). These components can be considered as components in a Cartesian coordinate system. Each sample point collected in the AUT corresponds to a point in the XY plane for each sideband and the angle of each point with respect to the horizontal corresponds to the phase of both oscillators in quadrature. To demonstrate this, an array of periodic aluminum square patches of 2.2 μm in size on a 3 μm pitch was placed under the s-SNOM setup in pseudo-heterodyne mode and the distribution of the first and second sidebands was measured. The LIA possesses a functionality denoted as *zeroing*, that allows the locking of the oscillators to the phase of the signal, i.e., making the phase angle θ either 0, π or $-\pi$.
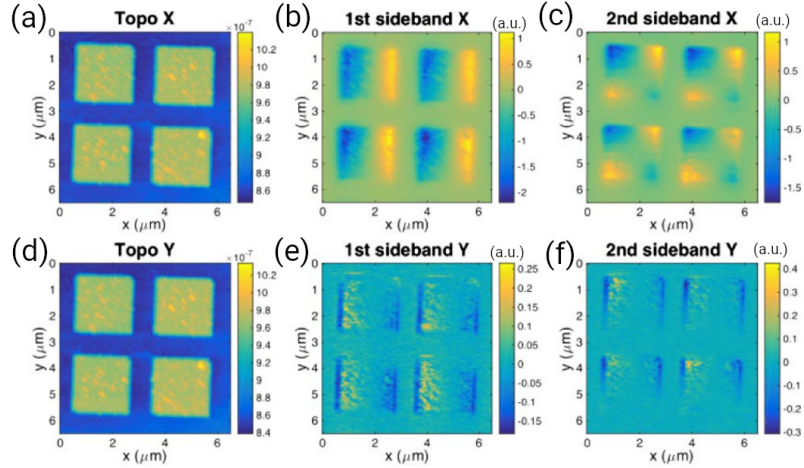
Figure 3.2: (a) and (d) show the AFM topographies for the collection of the X and Y components for data set A, respectively (units in color scale are given in m). (b) and (c) show the X components for the first and second sidebands, respectively. (e) and (f) show the Y components for the first and second sidebands, respectively.

A first measurement was obtained employing the zeroing function (data set A) and a second measurement was obtained in which the zeroing was not used (data set B). For the data set A, two s-SNOM scans were performed, one to obtain the X component of the first and second sidebands simultaneously, and the second one to obtain the Y

components. Fig. 3.2 shows the respective AFM topographies and sidebands for data set A. These topographies allow discrimination between the substrate and the square patch, so in the sideband scans, the pixels corresponding to the patch can be separated from the rest when plotted in the XY plane. These plots are shown in Fig. 3.3, where the signal corresponding to the resonant patches is in red and to the substrate is in blue. Plots in 3.3(a) and 3.3(b) show the original sideband signals retrieved form the LIA for the first and second sideband respectively. These plots show that a large proportion of the data points lie close to the horizontal axis, which implies that the zeroing function makes the phase $\theta = 0$, aligning the signal distribution along the X axis. These plots reveal that the measured near-field is associated with the resonances of the metallic structures, while the substrate does not contribute to the near-field (the reason this is not zero can be attributed to noise).

Figure 3.3: Data cloud for the s-SNOM signals collected for data set A. (a) and (b) show the original data clouds as measured for the first and second sidebands, respectively. Plots (c) and (d) show the data only from the resonant structure, the mean of the cloud has been placed at the origin and straight green lines represent the directions of maximum and minimum variance of the data. Plots (e) and (f) show the data cloud rotated to align the maximum-variance direction with the horizontal.

A closer inspection of the data clouds shows that despite most of the data points lying along a straight line, this line is not horizontal. To quantify this tilt, a principal-component decomposition is applied [36]. Briefly, this analysis starts with finding the

center of mass (first-order moments) of the data obtained for the X and Y components for the substrate and the origin of coordinates is translated to this point. This is based on the assumption that the majority of the near-field interaction originates in the metallic structure while the substrate signal should be zero. Next, the data-cloud distribution of the sidebands can be characterized by the calculation of the covariance of the X and Y coordinates. Diagonalization techniques such as the principal-component analysis in two dimensions allow the calculation of the covariance matrix for the distribution of data points. This analysis results in the maximum and minimum variances (σ_{max} and σ_{min}, respectively) of the data, and their orientation β. For data set A, these variances are plotted as green line segments in Figs. 3.3 (c) and 3.3(d). The length of these segments are proportional to the root mean square variation of the data. As seen, the maximum variance and minimum variance directions are not exactly oriented along the X and Y axes. To compensate for this, the data cloud can be rotated around the origin by a rotation angle equal to the direction of of the largest variation. The resultant plots after rotation are shown in Figs. 3.3(e) and 3.3(f).

The signals from the first and second sidebands can now be extracted from the rotated data cloud, and these can be used to calculate the near-field generated by the resonant structures under test. The signal for the second harmonic and m-th sideband can be obtained form the X component, i.e. $S_{2,m} = X$. With the sideband signals, then Eqs. (3.11) and (3.13) can be used to find the modulus and phase of the near field. Fig. 3.4(c) and 3.4(d) show the retrieved near-field modulus and phase, respectively, when the X component is employed. In contrast, if the sidebands are defined as they commonly are, i.e. $S_{2,m} = R = \sqrt{X^2 + Y^2}$, then the near-field can be computed using Eqs. (3.11)-(3.13). The resultant modulus and phase maps are shown in Figs. 3.4(a) and 3.4(b), respectively. When comparing the phase maps obtained using the two methods, when employing the magnitude R of the sidebands, the whole
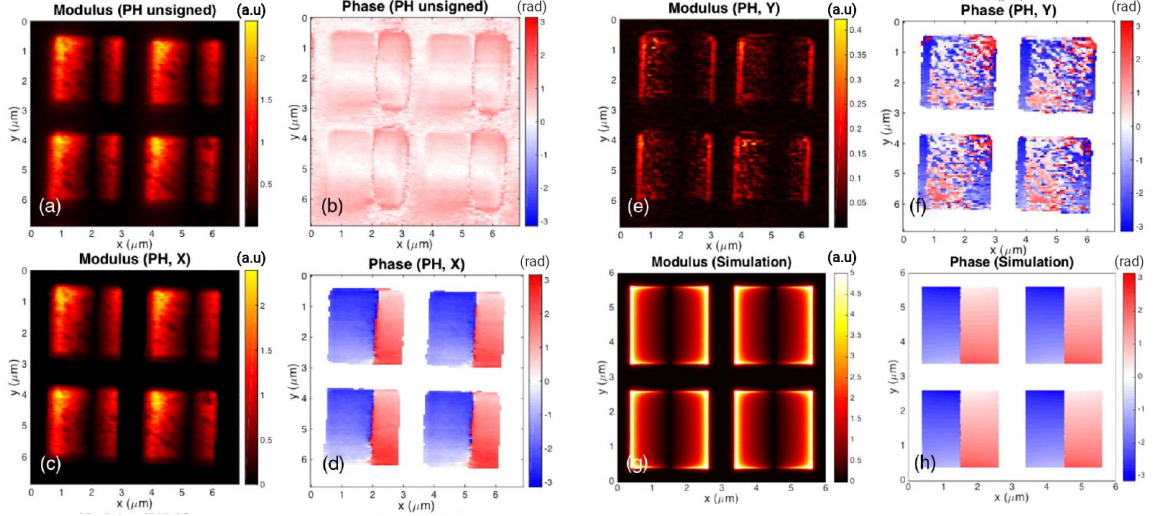
Figure 3.4: (a,c,e,g) near-field modulus and (b,d,f,h) phase for the square patches for data set A. Maps (a) and (b) correspond to the computed near-field from the unsigned sidebands. Maps (c) and (d) correspond to the near-field obtained from the rotated sidebands and the X component. Maps (e) and (f) were obtained from the Y component. Maps (g) and (h) were obtained from numerical simulations for the same structures.

range for the phase is not accessible, while for the case of employing the X component as the sideband signal the whole $(-\pi, \pi)$ range is accessible. The reason for this lies on the definition of the sidebands. If the sidebands $S_{2,m} = R$ then $S_{2,m} > 0$ so when computing the phase as defined in Eq. (3.13), the arctan function will return an angle constrained to the first quadrant. This is the case of the phase map in Fig. 3.4(b). However, when the sidebands are defined as $S_{2,m} = X$, they can be either positive or negative, so the calculated phase will be in any of the four quadrants. This result can be seen in Fig. 3.4(d), where the phase on the right half of each square patch is grater than zero while the left half is less than zero. This implies that the variance analysis and rotation of the data cloud for the sideband signals so that $|X| \approx R$ offers a full retrieval of the phase. As an example of what could happen if the orientation of the data cloud is not properly done, Figs. 3.4(e) and 3.4(f) show the near field obtained using the Y component for the sidebands, i.e. $S_{2,m} = Y$. These modulus and phase maps offer little insight on the near field and are predominately noise.

For validation purposes, the fields at the metallic square structures were solved for numerically using FEM methods, taking into account the same illumination conditions as in the experimental setup. The near-field distributions for modulus and phase obtained from the simulation are shown in Fig. 3.4(g) and 3.4(h), respectively. Although the simulated maps agree with the experimental data in Figs. 3.4(a) and 3.4(c), the simulated phase map in 3.4(d) has a better agreement with the phase expected from the simulations. This further confirms that the zeroing of the sideband signals and the consideration of the X component as sideband signal is an accurate method to measure the near-field on a metallic micro-structure.

In the case where the zeroing function for the signal angle is not available in the LIA, the variance analysis and rotation of the data cloud can be still applied when considering both the X and Y components of the sideband signal. This is the case of data set B, where the noise is greater than in data set A, and no zeroing procedure has been applied. Figs. 3.5(a) and 3.5(b) show the first and second sideband signals in the XY plane as obtained form the LIA. In both plots, the data is oriented in an oblique direction β with respect to the horizontal. This orientation can be corrected by centering based on the substrate data and subsequent rotation to align the data along the X axis. Figs. 3.5(c) and 3.5(d) show the resultant sideband signals after rotation correction. Once corrected, the near-field can be calculated using the X component of the sidebands. The resultant modulus and phase maps are shown in Fig. 3.6(a) and 3.6(b), respectively. When comparing these results to those from data set A, similarities between the distributions of the modulus are observed. However at the bottom portion of the square patches from data set B the phase is departing from the from the results obtained from data set A. This difference in the map can be explained when considering the effect of the global phase Ψ_G, which impacts the location of the 2π-phase-wrapping boundary over the sample. Fig. 3.6(c) shows the phase map when the sideband signals are considered as the modulus of the sideband

components (i.e. $S_{2,m} = R$), procedure which does not retrieve the phase correctly.
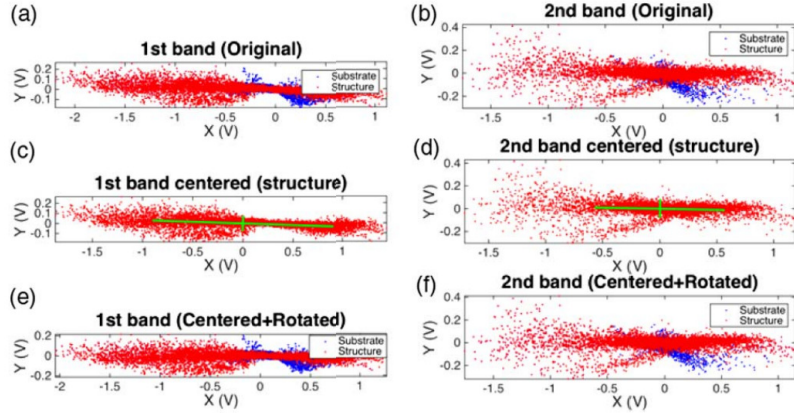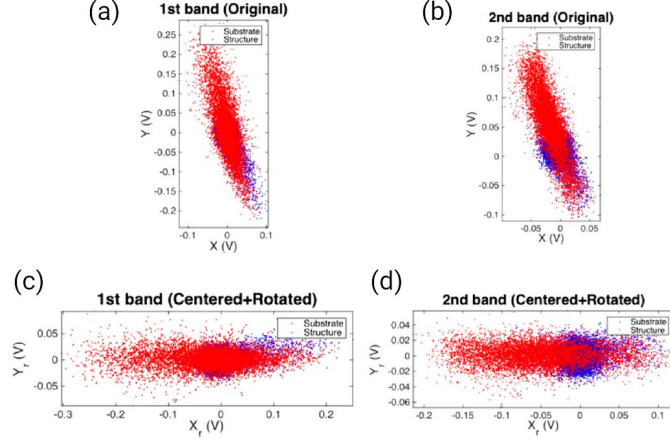

Figure 3.5: Data cloud for the s-SNOM signals collected for data set B. (a) and (b) show the original data clouds as measured for the first and second sidebands, respectively. Plots (c) and (d) show the data cloud rotated to align the maximum-variance direction with the horizontal.
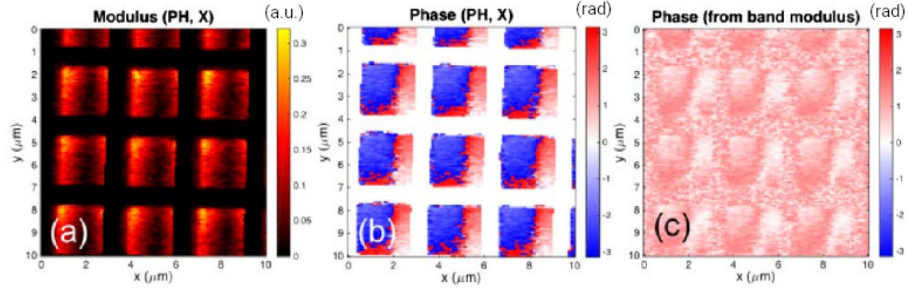
Figure 3.6: (a) Near-field modulus and (b) phase, corresponding to the square patches structures for data set B when considering the corrected X component. Plot (c) corresponds to the phase calculation considering both X and Y components.

A way to characterize the impact of the variance analysis described in this section is to consider the amount of maximum variance and how it compares with the total variance. The parameter $w_{\max}$ is defined as

$$w_{\max} = \frac{\sigma_{\max}^2}{\sigma_{\max}^2 + \sigma_{\min}^2}. \tag{3.14}$$

When $w_{\max}$ approaches unity, the data cloud is aligned in a definite direction and the

rotation of it gives a good alignment along the horizontal direction. The X component then approximates the magnitude R better and the Y component approaches to zero. Table 3.1 lists the rotation parameters β and $w_{\max}$ for the data sets A and B. Data set A has a higher $w_{\max}$ for both sidebands than data set B, which is due to noise in the sidebands that cause higher variance of the data in the Y component after rotation. This means that noisy signals can still be used to retrieve the modulus and phase along a metallic structure, however stronger and low-noise s-SNOM signals will result in more accurate near-field measurements when using the zeroing function and considering the X component for computation purposes.

Table 3.1: Rotation angle β and the variance parameter $w_{\max}$ for the respective data set considered when studying the square patch structure. Subscripts 1 and 2 indicate the first and second sidebands, respectively.

Data set	β_1 (deg)	$w_{\max,1}$	β_2 (deg)	$w_{\max,2}$
A	-1.96	0.9945	-1.45	0.9812
B	-75.18	0.9370	-71.65	0.9407

3.1.4   Global Phase and Reference Mirror Position

Equation (3.12) includes the explicit dependence of the phase of the near field $\phi(x, y)$ and the global phase Ψ_G. This global phase is related to the mean position of the vibrating mirror at the interferometer. This mean position can be easily changed by varying the DC component driving the piezoelectric stage that the mirror is attached to. In the s-SNOM setup, the AUT is moved under a static illumination, and the position of the vibrating cantilever is fixed. Therefore, the global phase should not change over the whole scanning window. From the measurement point of view, and considering the relationship between these phase terms given by Eq. (3.12), any change in the phase offset Ψ_G should be compensated by the phase contribution retrieved from the arctan evaluation of the sideband signals. Although the relative phase variations between different locations on the sample remain the same, the actual

phase map could differ when considering different mirror positions, mainly because the location on the sample where the phase is wrapped within the usual 2π range varies with Ψ_G, as happens when comparing the phase maps obtained from data sets A and B. To analyze this, the complex electric field E_z can be represented in the complex plane where the two sideband signals retrieved from the s-SNOM represent the real (+2nd band) and imaginary (−1st band) parts. The resulting plot can be interpreted as a data cloud in which each point corresponds to a position in the sample. In this representation, the definition and location of the origin are important. As previously, the data corresponding to the substrate and metallic patch can be distinguished so the substrate data can be used to center the data cloud around the mean value. This plot is shown in Fig. 3.7(a).
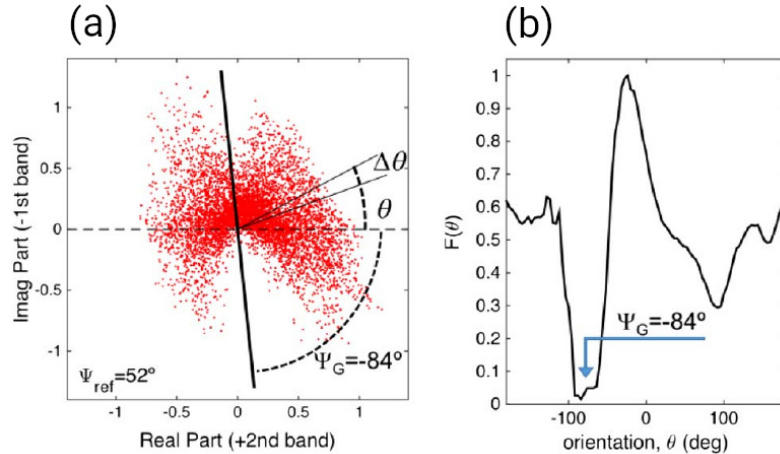
Figure 3.7: (a) Distribution of the near-field for a specific position of the reference mirror. Each point defines the modulus and phase of the electric field at a given location on the sample. (b) Angular representation of the normalized function $F(\theta)$ for the mirror position presented in plot (a).

For each point in the E_z data cloud, its distance to the origin is proportional to the modulus of the field and its angle $\Phi(x, y)$ with respect to the horizontal is related to the phase $\phi_{(x,y)}$ through Eqs. (3.12) and (3.13). So to relate the orientation of the cloud and the mirror position, a similar analysis can be applied to obtain the angle of maximum or minimum variance. However, due to the special shape of the data

cloud, an additional parameter is introduced in this analysis. Let $F(\theta)$ be the mean of the modulus for those data points contained in an angular sector $\Delta\theta$ as a function of the orientation θ of this angular sector. Mathematically, this parameter is given by

$$F(\theta) = \frac{1}{M_{[\theta,\theta+\Delta\theta)} \sum_{j\in[\theta,\theta+\Delta\theta)}} |E_{z,j}|, \qquad (3.15)$$

where the sum is carried out within the angular sector $[\theta, \theta + \Delta\theta)$, and $M_{[\theta,\theta+\Delta\theta)}$ is the number of points within this angular sector. For the data sets analyzed, $F(\theta)$ presents two local minima located about 180° apart. By selecting the appropriate minimum, it is possible to define the orientation of the data cloud. Fig. 3.7(a) shows the data distribution for a single position of the mirror as well as the orientation of the cloud with a straight black line. 3.7(b) shows the parameter $F(\theta)$ (normalized) as a function of the angular range with the angular sector $\Delta\theta = 4°$.

Twelve s-SNOM measurements were performed at different reference mirror positions l. By selecting a mirror position l_0 as reference, then a displacement from the reference can be defined as $\Delta l = l - l_0$. So for each displacement, a reference angle can be defined as $\Psi_{\text{ref}} = 4\pi\Delta l/\lambda$. For this set of measurements, the sample used to obtain the near fields was the same that comprises four metallic square patches similar to the ones previously considered. In each measurement, the zeroing function on the LIA was used and the X components of the first and second sidebands were collected. This is based on the results found in the previous section, which suggest that collecting the X component after zeroing offers an accurate method to find the near field. Figure 3.8 shows the calculated global angles for the twelve mirror positions considered. A shift of 229° has been made to make the fitted straight line pass through the origin. The red line represents the best straight line fitted to the data, constrained to a fixed value of the slope equal to -1. This confirms that the global phase term is related to the reference mirror position l, and is given by $\Psi_G = 4\pi\Delta l/\lambda$. The slope value is the origin of the negative sign in Eq. (3.12).
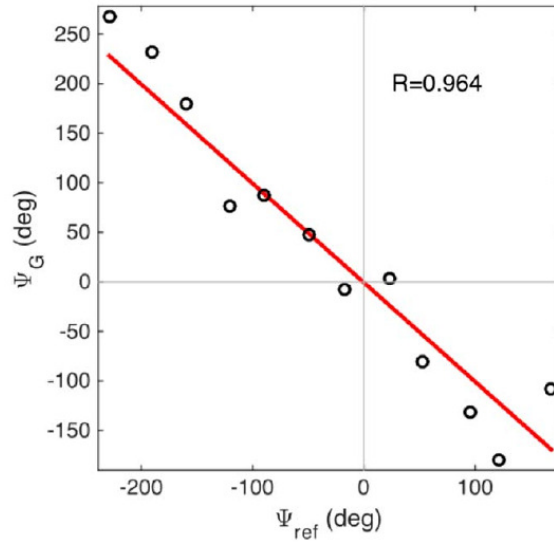
Figure 3.8: Calculated phase Ψ_G for different reference mirror positions.

In summary, the analysis of the data cloud when combining the X and Y components for the sidebands registered by the LIA can provide a simple method to improve the reliability and quality of near-field measurements of the modulus and phase in the s-SNOM setup.

CHAPTER 4: DISCRETE BOW-TIE NANOANTENNAS

In this chapter a discrete bow-tie antenna design is introduced and studied. The contents of this chapter were originally published in reference [37]. The discrete bow tie is based on the traditional bow tie design, where discrete elements are used in order to increase the near-field enhancement above the antenna and to widen its frequency response [38]. The performance of the proposed discrete bow-tie plasmonic nanoantenna is modeled, fabricated and its near-field response is investigated in this chapter.

4.1   Numerical Simulations
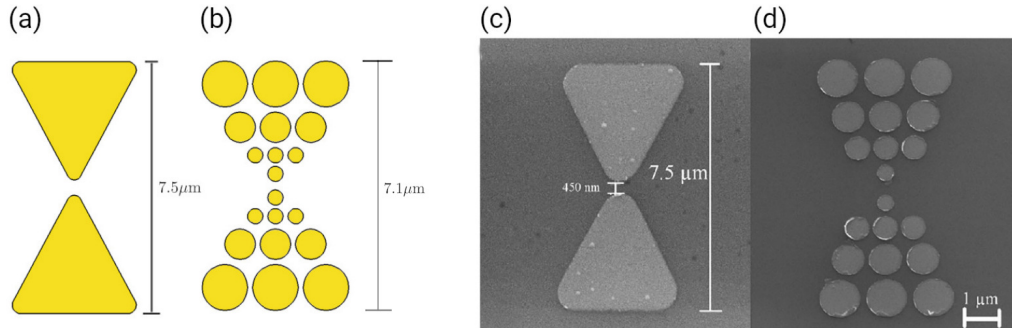
Figure 4.1: Antenna designs used for the modeling of the (a) classical and (b) discrete bow-tie antennas.

Finite element simulations were performed using COMSOL Multiphysics (RF module) by launching a linearly polarized plane wave at 60° angle of incidence to simulate the conditions of the s-SNOM setup. The geometry of the classical and discrete bow-tie antennas are shown in Figs. 4.1(a) and 4.1(b). As seen, the discretization of the bow tie was done with a series of circles with varying sizes that fill the area of the antenna. The dimensions of the classical antenna were chosen for resonance at

a wavelength of 10.6 μm. The classical bow tie has a length of 7.5 μm and a 450 nm gap, and the discrete bow tie has a length of 7.1 μm and a 300 nm gap. The z-component of the electric field E_z (normal to the bow-tie plane) is evaluated at 20 nm above the antenna. Simulations were performed by varying the polarization and frequency of the incident electromagnetic wave form 24 to 100 THz (or 3 to 12.5 μm in wavelength).
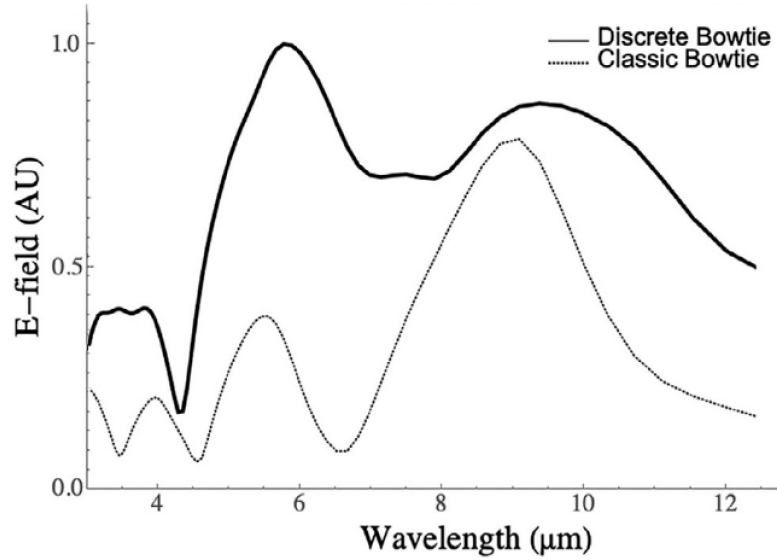
Figure 4.2: Plot of the computed magnitude of the electric field at the feedpoint gap of the classical bow-tie nanoantenna (continuous line) and discrete bow-tie nanoantenna (dotted line) as a function of the wavelength when the incident wave has vertical polarization. The magnitude of the field has been normalized to the maximum of the discrete bow-tie antenna.

Figure 4.2 shows the computed simulated electric field at the feedpoint gap of the classic and discrete bow-tie antennas as a function of wavelength. The feedpoint in the discrete bow-tie antenna was taken as the gap at the geometrical center of the discrete antenna. Finite-element computer simulations show that in the discrete antenna the bandwidth, considered to be when the E-field at the gap decreases to half its maximum value, increases from approximately 7.5 to 10.5 μm (or 28.6 to 40 THz in frequency) for the classical bow-tie antenna to 4.5 to 12 μm (or 25 to 66.6 THz in frequency) in the discrete bow-tie antenna. It is also worth noting that the

classical bow-tie antenna has a larger relative peak response at the main resonance than the discrete bow-tie antenna, which might be of interest for frequency-specific applications.

Figure 4.3 shows the magnitude of the electric field at the central gap of the bow ties as a function of polarization of the incident wave. As seen in the plot, the polarization dependence is more pronounced for the discrete antenna compared with its classical counterpart. As expected, the magnitude of the field is larger for polarization state along the axis of the antenna (at 90° and 270°), but it is worth noting that this enhancement is approximately four times higher for the discrete antenna compared to the classical design.
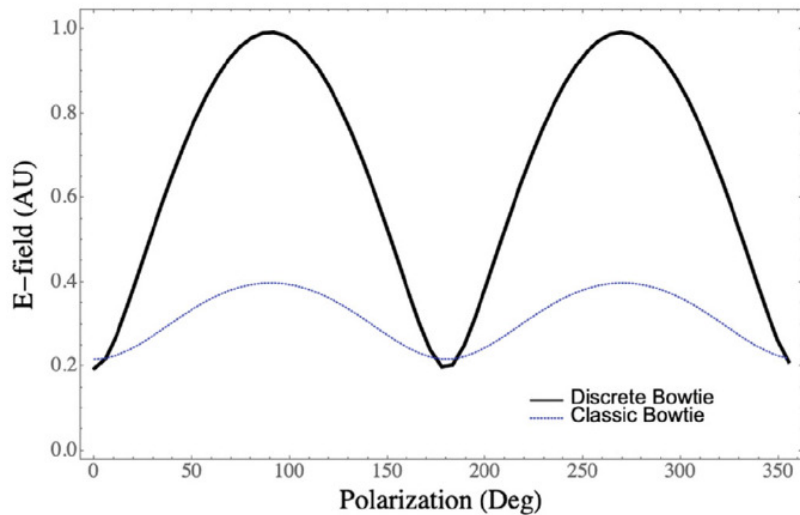
Figure 4.3: Magnitude of the electric field at the gap of the classical and discrete bowtie nanoantennas as a function of the angle of polarization for an incident plane wave at 28.3 THz (10.6 μm in wavelength).

Figure 4.4 shows the computed magnitude of the z-component of the E-field distribution 20 nm above the antenna plane for classical and discrete nanoantennas, for different polarizations of the incident wave. Considering the whole antenna structure, it can be seen how different polarizations generate E-field hotspots at different locations in the antenna. This is especially noticeable in the discrete bow tie nanoantenna where a large number of hotspots are seen for various polarizations. The plots

show the magnitude of the field, and the 45° polarization case is, as expected, a superposition of the horizontal- and vertical-polarization cases.
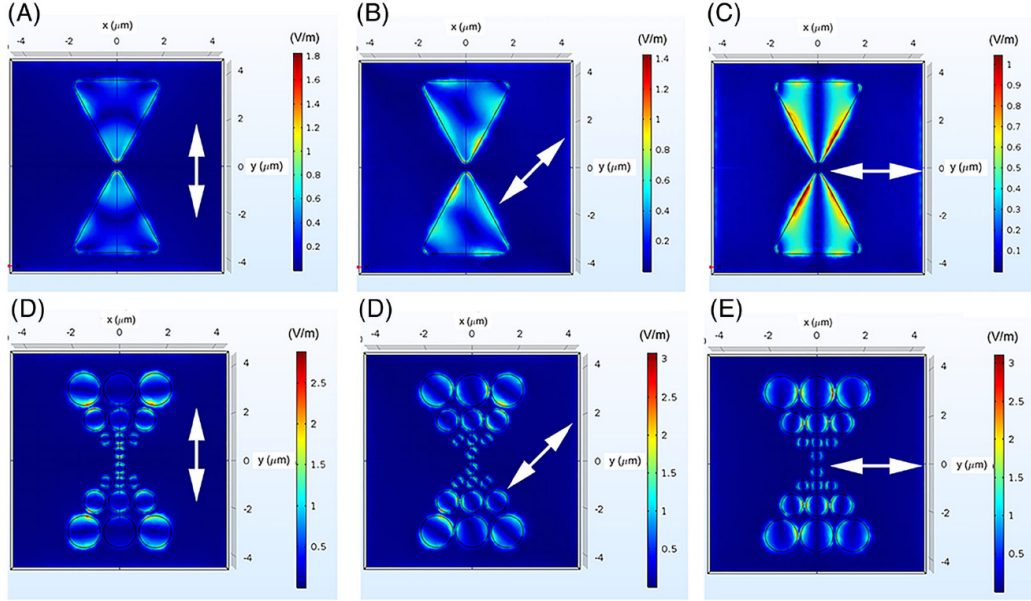
Figure 4.4: Computed z-component of the E-field at the above the antenna plane for the classical and discrete bow-tie nanoantennas. (A-C) show the field distribution for the classical bow-tie antenna, while (D-F) correspon to the discrete bow-tie antenna. Vertical, diagonal and horizontal arrows indicate the polarization state (linear vertical, at 45° and horizontally polarized respectively) of the incident plane wave with frequency of 28.3 THz (10.6 μm in wavelength).

4.2   Experimental Results

The bow-tie antennas were fabricated using standard a electron-beam lithography and metallization procedure as outlined in Chapter 2. Briefly, antennas were fabricated on a Si wafer with 300 nm of SiO_2 as thermal and electrical isolator. The fabrication procedure used was the following: 300 nm of polymethyl methacrylate was spun on the substrates and then baked at 180°C for 15 minutes. Patterning was done with a Raith ELPHY Quantum (Raith America Inc., Ronkonkoma, New York) lithography system, installed in a FEI Inspect F50 field-emission scanning electron microscope. The antenna patterns were written using an electron-beam exposure of 30 keV and an area dose of 250 μC/cm^2. Development was performed by soak-

ing the samples in an MIBK:IPA solution for 75 seconds. Then 50 nm of gold was deposited by RF sputtering. The devices were left in an acetone bath overnight for lift-off. Figure 4.1(c) and 4.1(d) show scanning electron micrographs of the fabricated structures.
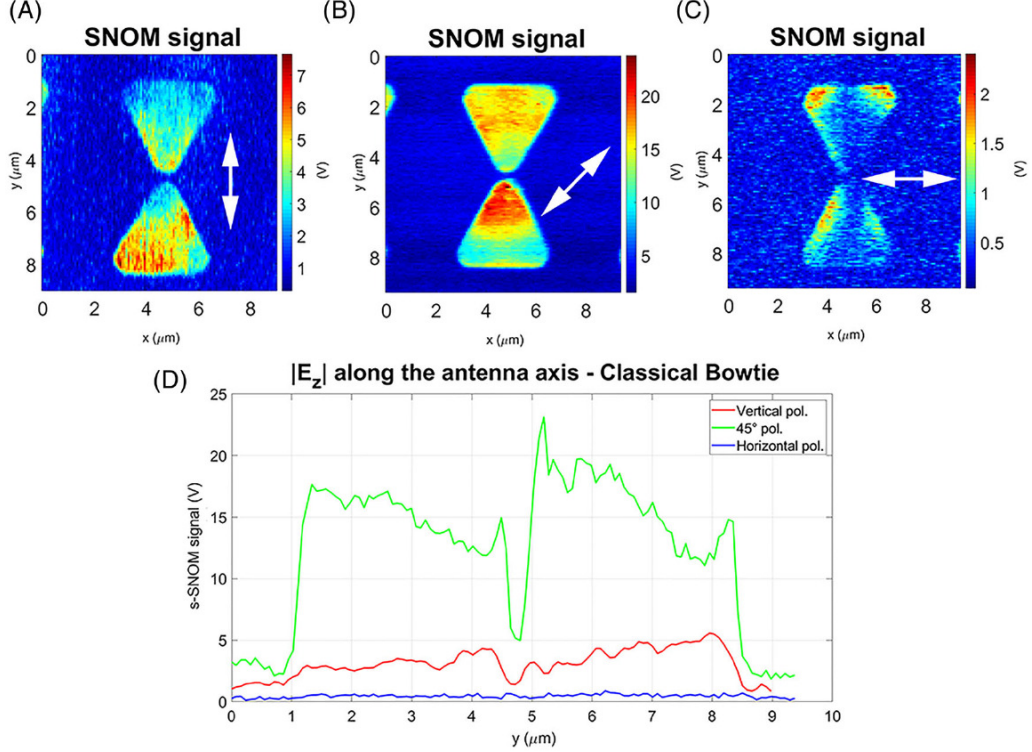
Figure 4.5: Experimental near-field s-SNOM measurements for the classical bow tie antenna. White arrows indicate the polarization orientation for the incident wave: (A) vertical, (B) 45° and (C) horizontal. (D) s-SNOM signal along the vertical axis of the antenna for the vertical, 45° and horizontal polarization measurements.

The fabricated antennas were tested under the s-SNOM, operating in pseudohetero-dyne scheme, to measure the near-field distribution. The method used to obtain the near field was the same as was used for the square patches as described in Chapter 5. The near-field maps measured on the classical bow tie are shown in Fig. 4.5. Inspection of the field distribution along the antenna suggests that under vertically polarized illumination, the field strength is greater near the gap in the top half of the antenna, and it tends to be strong along the edges. When illuminated with linearly

polarized radiation at 45°, the field is stronger predominantly near the antenna gap. Under horizontal polarization, the near-field strength is higher along the left and right sides of the bow tie while it is lower along the longitudinal axis of the antenna. Fig. 4.5(D) shows the field profile along the antenna axis for the three polarization cases considered. Comparing the signals along the antenna axis, the near-field at gap for 45° polarization is five times greater than the vertical polarization case.
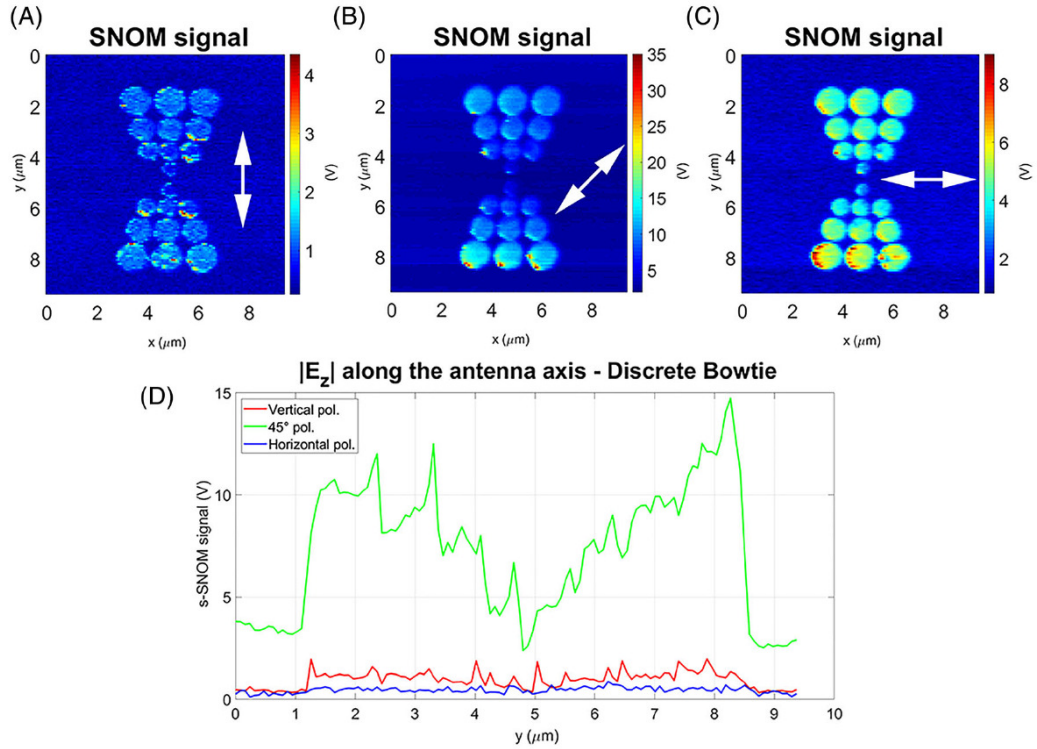
Figure 4.6: Experimental near-field s-SNOM measurements for the discrete bow-tie antenna. Near-field maps under: (A) vertical, (B) 45° and (C) horizontal polarization. (D) s-SNOM signal along the vertical axis of the antenna for the vertical, 45° and horizontal polarization measurements

Figure 4.6 depicts the s-SNOM measurements on the discrete bow ties. The near-field maps shows that hotspots are distributed over a greater region of the antenna compared to their classical counterpart. When illuminated with vertically polarized radiation, the hotspots are predominantly located in the interior edges of the discs composing the bow tie. With linearly polarized radiation at 45°, the near-field strength is greater at the 8 o'clock position on various discs and the three in the

bottom exhibit localized hotspots. With horizontally polarized radiation, the near field is higher toward the left edge of multiple discs. Analyzing the signals along the antenna axis, we see that for 45° polarization the near field is greater at the upper and lower ends of the antenna, while at the gap the field reduces to about 33%. Additionally, at this polarization, the near field at the antenna edges can reach values 10 times greater than the field on the discs near the gap.

In general, the near-field measurements on both bow ties agree with the predictions from simulations. The differences between the measurements and the simulations, such as the hotspot locations and asymmetry of the field distribution, are likely caused by the finite spatial resolution of the measurement apparatus and by residual misalignments in the positioning of the antennas when measuring them. A relevant finding from the experimental results is the presence of a residual response over most of the metallic area that constitutes the bow-tie antennas. In particular, the discrete devices exhibit a broader spatial distribution of hotspots across the active area of the antenna structure and the magnitude of the electric field is greater than in the classical bow tie. While the exact positions of these hotspots vary with the incident polarization, they reliably occur at the edges of the disc elements. These results represent a confirmation of the hypothesis that discretization of the geometry can enhance antenna parameters. Numerical simulations suggest that this simple discretization into finite discs broadens the antenna bandwidth, while experimental results suggest that this discretization increases the hotspot density across the metallic structure for different orientation of polarization of the incident wave. This feature is of potential interest for applications where an extended region of electric-field enhancements is desired, such as in surface enhanced Raman spectroscopy, biosensing, and plasmon generation.

CHAPTER 5: IMPEDANCE MATCHING

Infrared detectors are devices that convert electromagnetic waves at infrared frequencies into a measurable physical quantity [39]. These detectors are widely use in defense, thermal measurement, and imaging applications [40, 41, 42]. Infrared detectors are divided into two main classes: thermal and photon detectors [43]. Thermal detectors operate based on the the fact that when electromagnetic radiation is incident into a material, its temperature will change, as a result variations of physical properties of such material can be observed and used to generate electrical output. Bolometers are thermal detectors, for which changes in temperature cause a change in electrical resistance. This class of detectors have modest sensitivity, relatively slow response and are inexpensive.

In photon detectors, incoming electromagnetic radiation is detected by excitation of electrons in the material, which causes an electrical output [43]. Photon detectors are commonly made based on semiconductors, materials that are selective in the wavelength of operation. These detectors have optimal signal-to-noise ratio, but typically require cryogenic temperatures. This limitation makes photon detectors inconvenient for widespread applications because they are bulky, heavy and expensive to operate.

A method to overcome the limitations imposed by infrared photon detectors involves the use of an antenna coupled to such detector. The concept of an antenna coupled to a metal-oxide-metal (MOM) diode was modeled by Sanchez *et al.* in the context of infrared detectors [44]. In this approach, incident radiation is coupled from an electromagnetic wave into an antenna, and the MOM diode acts as the load for the antenna. Therefore, this circuit can be characterized by the diode resistance R_D and

capacitance C_D in parallel, which is in series with the resistance r of the metal lead for the diode. The antenna can be described as a series connection with impedance $Z_A = R_A + iX_A$, where R_A is the antenna resistance and X_A is its reactance. So for the antenna-diode circuit, the RC time constant is given by the equivalent resistance and the diode capacitance. So the cut-off frequency is

$$f_c = \frac{1}{2\pi RC} = \frac{R_A + r + R_D}{2\pi(R_A + r)R_D C_D}. \tag{5.1}$$

To reduce the response time of the diode the capacitance of the diode C_D must be small. Assuming the capacitor can be modeled as a parallel-plate capacitor, the capacitance is proportional to the junction area and inversely proportional to the thickness of the dielectric. MOM diodes can have an oxide thickness of 2.5 nm and an equivalent resistance of 1 kΩ, so this diode requires a junction area smaller than 75 nm $\times$75 nm to attain a cut-off frequency high enough to rectify at infrared frequencies [14].

However the efficiency of the power transmission in between the antenna and the diode load depends on the impedance matching between both elements. Maximum power transfer occurs when the resistance of the diode R_D is equal to the resistance of the antenna R_A. Typical dipole antennas have an input resistance in the order of 75 Ω [18], which implies there is a significant impedance mismatch between the antenna and diode. Therefore a method that could either tune the diode impedance without the necessity of modifying the diode itself, or increase the antenna impedance to match the diode is of interest. Section 5.1 addresses the first scenario making use of a DC bias across the diode, and Section 5.2 introduces two high-resistance antenna designs for better match to a diode.

5.1   Biasing Metal-Oxide-Metal Diodes

Previous work demonstrated the possibility of changing the operating point on the $I-V$ curve on a infrared sensor coupled to a dipole antenna by applying a voltage bias [45]. The origin of this bias comes from the IR radiation incident into the antenna, which induces an AC voltage across the infrared sensor, and it has been shown that the detector response depends on the bias. This means that the impedance of the detector can be tuned via the applied bias. The implementation of a MOM diode as a load has been studied and the tailoring of the $I-V$ characteristics of such device was proven successful via controlling process parameters for fabricating the oxide layer of the diode [14]. This section combines these two approaches by studying a MOM diode as antenna load and analyzing the near-field response under DC bias to test if this coupling can control the IR response of the device.
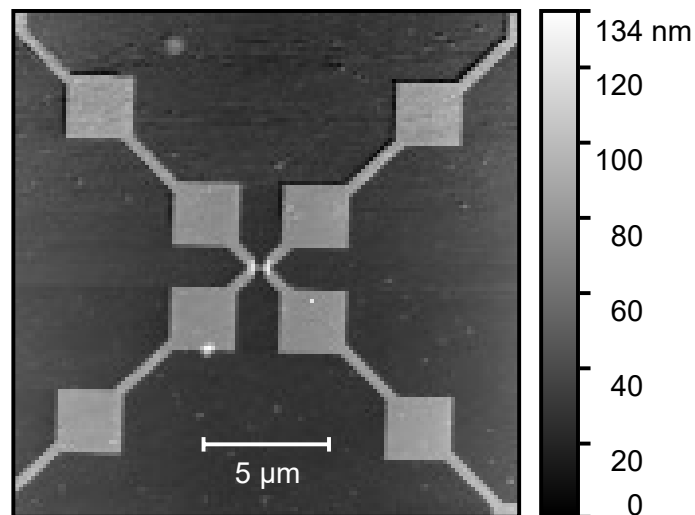
Figure 5.1: AFM topography of the antenna-coupled diode. Diode is located at the central intersection of the diagonal transmission lines.

In the antenna-coupled diode as infrared detector studied, the antenna consists of transmission line with a series of square patches arranged diagonally at $+45°$ and $-45°$, and at the intersection a MOM diode is placed. Fig. 5.1 shows the geometry of the antenna. The structure was designed and fabricated by an industry collaborator.

The s-SNOM was used to test the device as DC bias is applied.

Before the testing, first the device pads were wire bonded to a chip holder to provide the external DC bias. Wire bonding was done using a WestBond Manual Wedge Bonder (Model 7476D). Ten antenna-coupled diodes were wire bonded. Fig. 5.2 shows the structures after wire bonding. Further details on the parameters and procedure used for the wire bonding are presented in appendix B.
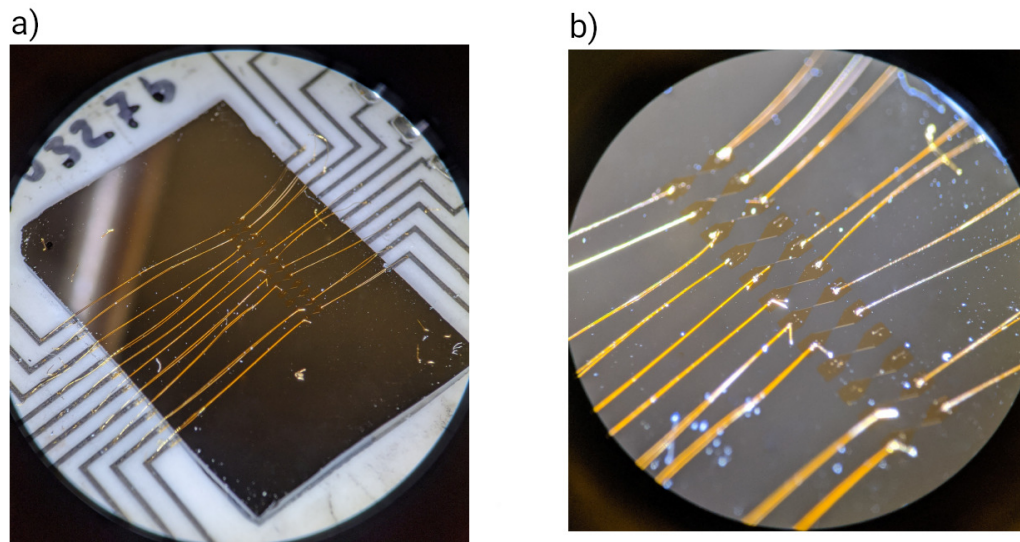
Figure 5.2: a) Photography of the wire bonds connecting the antenna pads to the chip carrier pads. b) Photography at higher magnification of the antenna-coupled diodes that were wire bonded.

To test the response of this device under infrared excitation, the s-SNOM was used to study the near-field distribution along the antenna when DC bias is applied. The s-SNOM maps along the structure were collected as bias was applied while infrared radiation was incident upon the antenna. This bias ranged from 0 mV to 50 mV, and the infrared radiation was linearly polarized along the x-axis and at a 60° incidence angle. The near-field maps, shown in Fig. 5.3, show that the antenna structure exhibits high near-field concentration at the corners of the lateral sides of the square patches and along the transmission lines.

When analyzing the fields along the transmission lines a standing wave pattern is
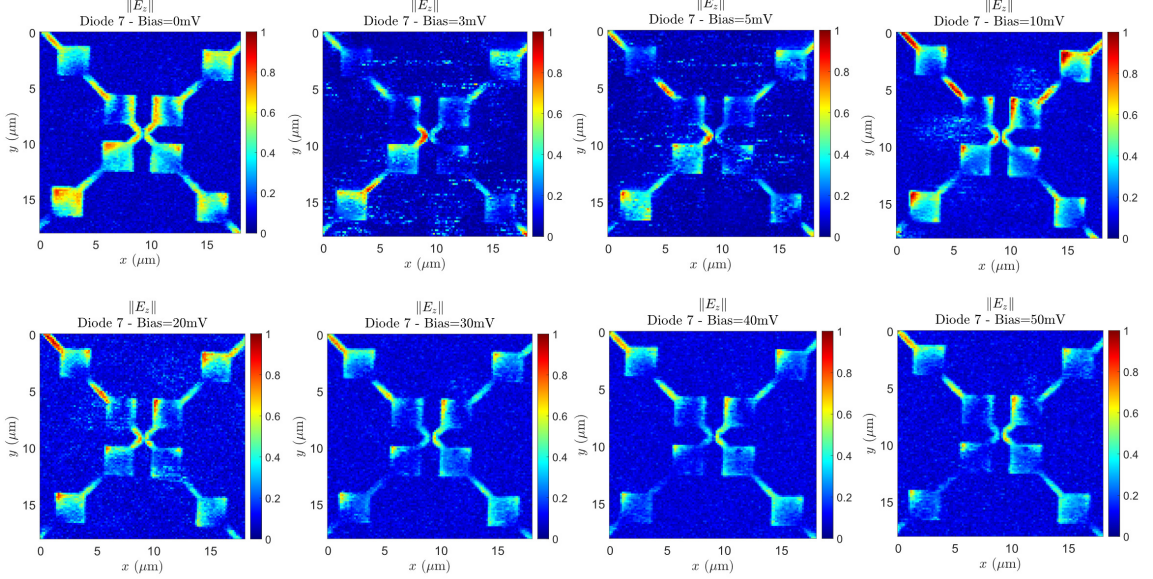
Figure 5.3: Collected s-SNOM depicting the magnitude of the near-field distribution on the antenna-coupled MOM diode for different applied DC bias. Maps are normalized to the maximum value of the field magnitude.

observed for the different biases applied. The distribution of the fields change as the DC bias increases. To quantify these variations, the fields along the $+45°$ and $-45°$ diagonals are extracted and studied as a function of the position. Fig. 5.4 shows the magnitude of the near field for each bias applied across the device, for both the $+45°$ and $-45°$ diagonals. Since the field patterns exhibit oscillatory behavior, a non-linear least squares fit is applied to each data set, for which the equation to fit is given by

$$y = Ae^{-\alpha x}\sin(kx + \phi) + D, \tag{5.2}$$

where the parameter A is related to the amplitude, α provides the attenuation of the current wave, k is the propagation constant, ϕ is the phase shift and D is a constant. The resultant fits are shown in Fig. 5.5. The field patterns along the $-45°$ diagonal are in phase, as their peaks and valleys occur at approximately the same positions. However this is not the case for the fields along the $+45°$ diagonal, for which there is a phase shift dependent on the bias voltage.
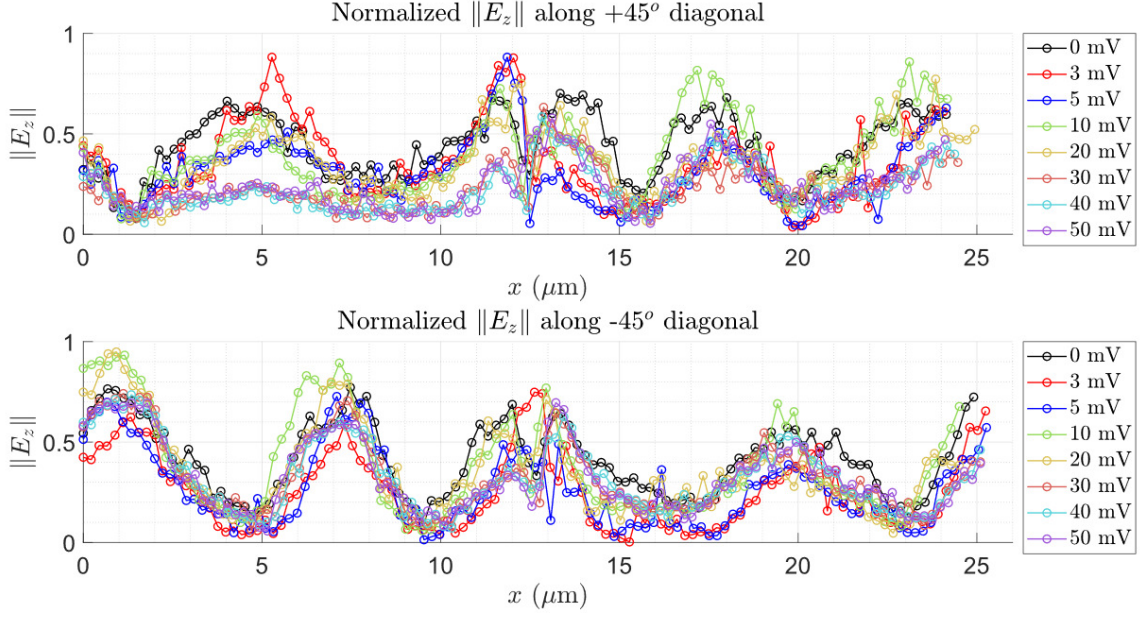
Figure 5.4: Magnitude of the standing wave along the +45° diagonal line (up) and along the −45° diagonal line (bottom) for different applied bias.
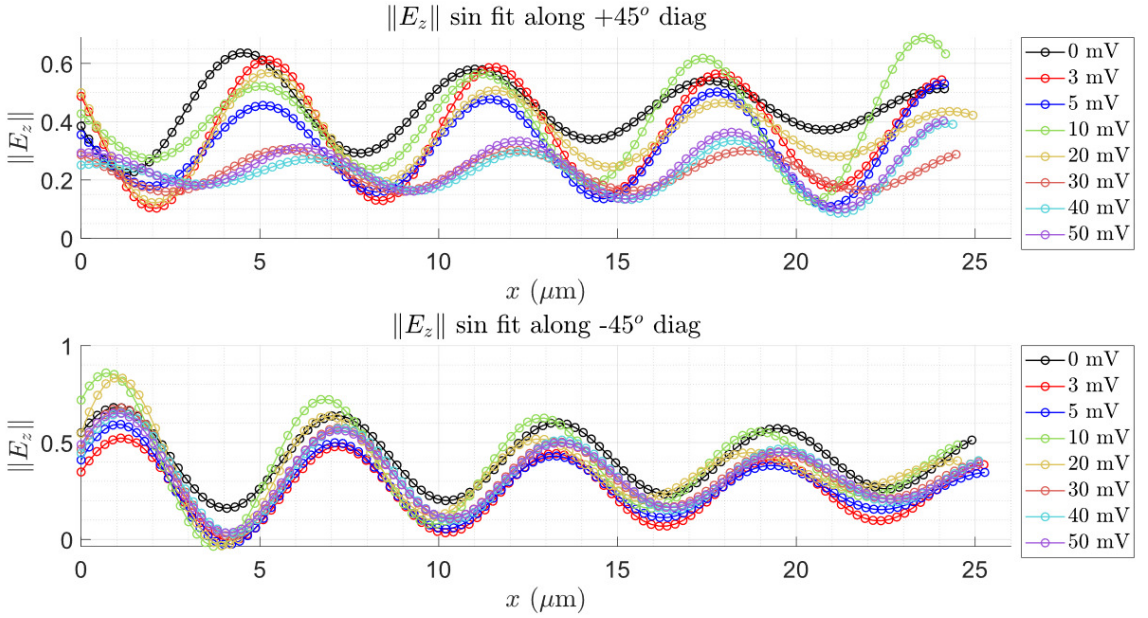
Figure 5.5: Non-linear fit of the magnitude of the standing wave along the +45° diagonal line (up) and along the −45° diagonal line (bottom) for different applied bias.

To understand the relationship of the bias and the phase shift, the phase ϕ is plotted as a function of the applied bias, shown in Fig. 5.6. For the −45° diagonal

lead line, there are no observable phase differences, while for the case of the $+45°$ diagonal lead line a bias-dependent phase change is observable. For the later case, the phase shift decreases linearly as the bias voltage increases. This implies that the field distribution along the antenna shifts as the bias voltage changes. The reason this occurs is because the external DC bias is tuning the resistance of the diode, and given that the power transfer between the antenna and the diode depends on the resistance match, then the transferred power changes with the bias. These changes in the power transfer are observable in the measured variations of the near field distribution along the antenna. This represents a first experimental observation of the DC bias across a diode controlling the current wave at infrared frequencies. Therefore this antenna-coupled diode under bias has the potential of offer a solution for diode resistance tuning and improve impedance matching of the elements. These phase changes with bias should be observed in both diagonal lead lines because the design is symmetric. Therefore fabrication imperfections that might impact the $-45°$diagonal line and break the symmetry could be responsible for the absence of phase shift on the field over this line.
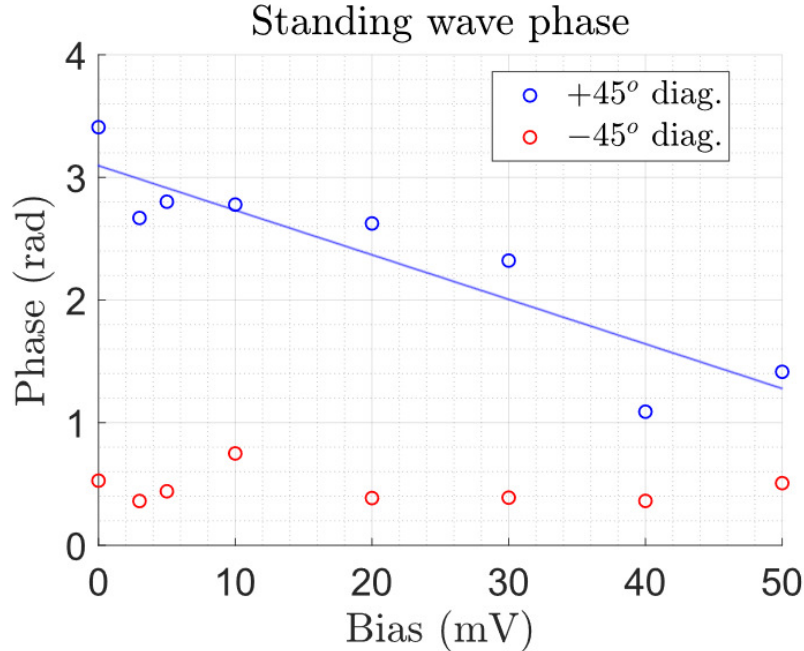
Figure 5.6: Plot of the standing wave phase ϕ as a function of the applied bias. In blue the data corresponding to the $+45°$ diagonal lead line and in red the data corresponding to the $-45°$ diagonal lead line.

5.2   Impedance Matching Antennas

The high impedance antennas studied in this section comprise first a modified folded dipole, and second a dipole-coupled t-match. These antennas are designed as microstrip antennas. A microstrip antenna consists of a metallic ground plane, a dielectric stand-off layer and the antenna. Zinc sulfide (ZnS) was chosen for the stand-off layer because it does not have loss bands in the 5 to 20 μm wavelength portion of the spectrum [46]. Chromium (Cr) was chosen for ground plane material because ZnS exhibits good adhesion to Cr [47]. Gold (Au) was selected as material for the antenna because of the low loss in the infrared [48]. To obtain the optical properties of these materials in the IR frequencies, a thin layer of ZnS was thermally evaporated (BOC Edwards Auto 306) on a silicon wafer, and a thin layer of Cr was e-beam evaporated (Kurt J. Lesker PVD 75), then the refractive index for both materials was measured using IR ellipsometry techniques as described in Chapter 2. Then the permittivity

and conductivity were calculated using Eqs. (2.10)-(2.12). The dielectric properties at 28.3 THz for these materials are listed in Table 5.1. The properties for Au were determined before by the same techniques [49].

Table 5.1: Relative permittivity and conductivity from ellipsometric measurements for the materials at 10.6 μm.

Material	ε_1	ε_2	σ
Cr	-259.23	312.38	4.92×10^5
ZnS	5.67	5.86×10^{-5}	0.092
Au	-4787	1630	2.56×10^6

Having determined the optical properties of the materials to use for the design, these same properties are input parameters in the numerical simulations to model real materials so that the predictions from the simulations are more accurate.

5.2.1   Numerical Simulations

To study the behavior of the antenna, it is modeled as an active device with a *lumped port* at its feed. In COMSOL, this feature is equivalent to a current source that induces an oscillating current onto the feed point. The lumped port is not only used as excitation port for the antenna, it also measures directly its impedance.

The following sections outline the models used to simulate the modified folded dipole and t-match antennas and the results obtained from these.

5.2.1.1   Modified Folded Dipole

The simulation domain consists of a rectangular volume, enclosing the stand-off layer, air layer and the antenna as shown in Fig. 5.7. The thicknesses of the ZnS stand-off layer and air layer are 1 μm and 3.65 μm, respectively. The Cr ground plane is approximated with the bottom face as a perfect electric conductor (PEC), because its thickness of 150 nm is several times the skin depth. The lateral faces are defined as periodic boundary conditions (PBC) to approximate an infinite stand-off layer and

ground plane surrounding the antenna.

Figure 5.7: Model layout for implementation of FEM for the modified folded dipole (units in m). The antenna domain is highlighted in blue, and units are given in m.

Figure 5.8: Model layout for the geometry of the modified folded dipole.

The geometry of the modified folded dipole is shown in Fig. 5.8. It consists of a folded dipole of length L with a gap of size G and stubs of length d. The dipole feed has a size $g_1 = 110$ nm and the width of the antenna is $w = 150$ nm. The antenna thickness is $t = 100$ nm. Numerical simulations in COMSOL are performed to compute the input impedance of this antenna as a function of the dipole length L, gap G and stub d at a frequency of 28.3 THz. A starting point for the length L can be determined using Eq. (2.1) for the effective wavelength. Assuming an antenna radius $R = w/2$, then $\lambda_{\text{eff}} = 7.15$ μm so the antenna length should be around $L = \lambda_{\text{eff}}/2 = 3.6$ μm. Then simulations with folded dipole lengths L ranging from 1.75 μm to 3.75 μm were carried out. Most of the designs do not exhibit high resistance at resonance, however three designs with lengths L of 2.25 μm, 2.50 μm and 2.75 μm show high resistance at resonance. Fig. 5.9 shows the simulated input impedance for these three designs of the modified folded dipole (MFD) as the gap size G changes. As seen in this plot, the maximum resistance (real part of the impedance)

gets smaller as the antenna length increases, while the gap size G at which resonance is achieved (imaginary part of impedance is equal to zero) increases with the dipole length. Table 5.2 details the dimensions of each design and the specific G for which the antenna exhibits resonance.
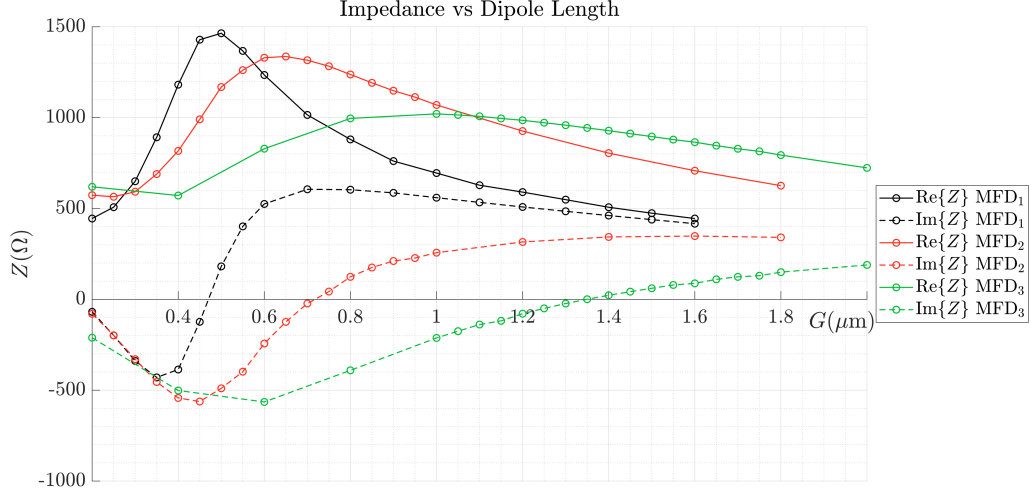
Figure 5.9: Computed input impedance for modified folded dipole (MFD) antennas 1, 2 and 3 (with parameter L equal to 2.25 μm, 2.50 μm and 2.75 μm respectively) as a function of the gap size G. Continuous lines represent the resistance (real part of the impedance) and dotted lines represent the reactance (imaginary part of the impedance).

Table 5.2: Geometry for the modified folded dipole (MDF) designs and the resistance R at resonance.

Design	L (μm)	d (nm)	G (μm)	R (Ω)
MFD_1	2.25	550	0.5	1464
MFD_2	2.50	450	0.7	1316
MFD_3	2.75	350	1.35	943

Simulations show that when selecting the appropriate dimensions for the folded dipole antenna, high input impedance at resonance with resistance around 1 kΩ, or higher, can be achieved. Therefore the designs in Table 5.2 are the base for the modified folded dipole antennas to fabricate and test experimentally.

5.2.1.2   T-Match

The simulation domain for the dipole antenna with t-match is analogous to the domain for the modified folded dipole. The same materials, boundary conditions and excitation elements were used as shown in Fig. 5.10. The overall antenna structure is shownin Fig. 5.11 as a dipole antenna of length L with a t-match network of length L_t connected to it. The metallic lines have a width of $w = 150$ nm and are separated by a distance $s = 100$ nm. The feed gap has a size $g = 110$ nm. Simulations for antenna length L ranging from 2.25 μm to 4.00 μm were performed, however only two designs exhibit useful resonance behavior. These two designs are for antenna length L of 3.00 μm and 3.27 μm. The computed impedances for these antennas are shown in Fig. 5.12. These results suggest that resonance occurs for a specific t-match length L_t. For the first antenna design with $L = 3.00$ μm resonance occurs at $L_t = 0.78$ μm, where the resistance is 920 Ω, while for the second antenna design with $L = 3.25$ μm resonance occurs at $L_t = 0.7$ μm, where the resistance is 850 Ω. These antenna dimensions are the base for the t-match antenna designs we fabricated and tested.
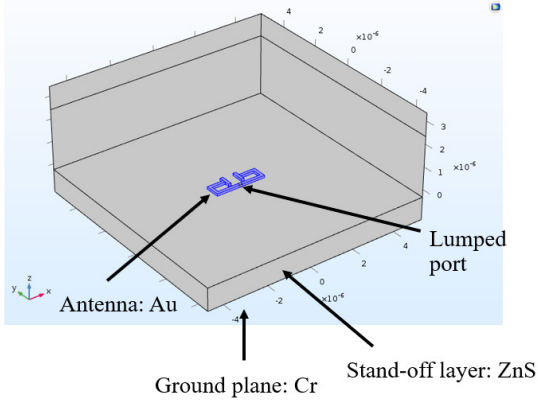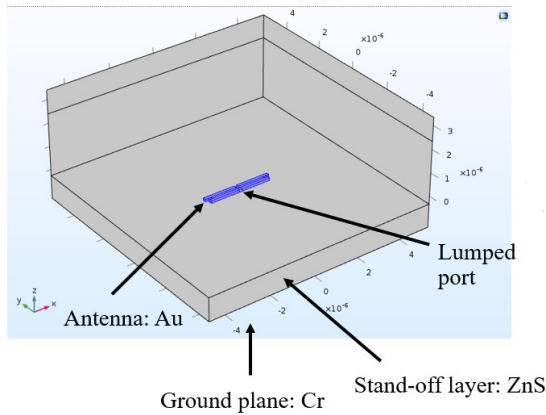
Figure 5.10: Model layout for implementation of FEM for the modified folded dipole (units in m). The antenna domain is highlighted in blue.
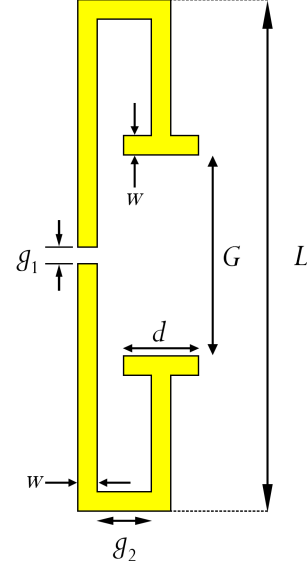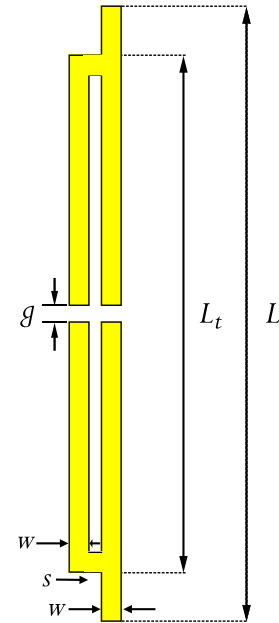

Figure 5.11: Model layout for the geometry of the modified folded dipole.
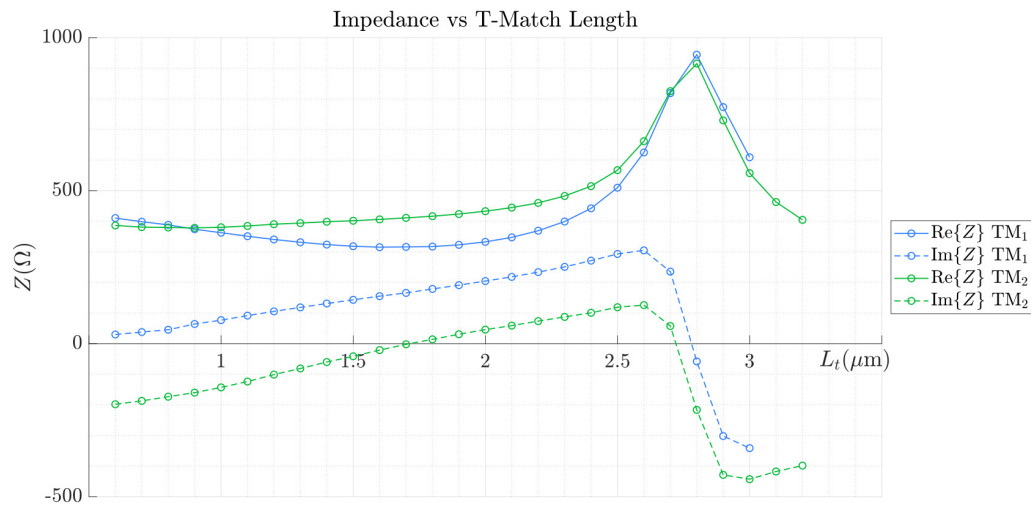
Figure 5.12: Computed input impedance for dipole antenna with t-match (TM) as a function of t-match length L_t. Designs TM_1 and TM_2 have a length $L = 3.00\mu$m and $L = 3.25\mu$m, respectively. Continuous lines represent the resistance and dotted lines represent the reactance.

5.2.1.3   Dipole-CPS-AUT coupling

In the simulations the excitation and measurement of impedance is provided by the lumped port element, however such element does not exists in the experimental context. So each antenna to test needs to be coupled to a system that allows the measurement of the impedance. It has been shown that a simple system to achieve this is a dipole coupled to a coplanar strip line (CPS) [24]. In this approach, an incident electromagnetic wave excites the half-wave dipole (designed to operate at the frequency of the incident radiation) generating a current along it. This current couples into the CPS, launching a propagating current wave originated at the dipole. The current wave generates a near field along the CPS which can be measured experimentally with the s-SNOM. With this experimental data, the antenna under test can be characterized and its impedance measured. However, this dipole-coupled CPS first has to be designed so it is resonant at infrared frequencies, specifically at 28.3 THz (or 10.6 μm in wavelength).

In section 2.1, it was established that the effective wavelength can be used to design a dipole that is operational in the infrared frequencies. To confirm this prediction, a microstrip dipole antenna was simulated in COMSOL, setting its length L as a free parameter and evaluating its characteristic impedance. The materials and boundary condition configurations for these simulations were the same as in the simulations described in the previous section. The dipole is made of gold, it is 100 nm thick, its width is 150 nm and its feed gap is 110 nm wide. The computed impedance results are shown in Fig. 5.13. Simulations suggest the dipole is resonant at $L = 2.0$ μm, and has an impedance of $Z = 30.48$ Ω. This dipole length is chosen for the designs as the input coupling structure.
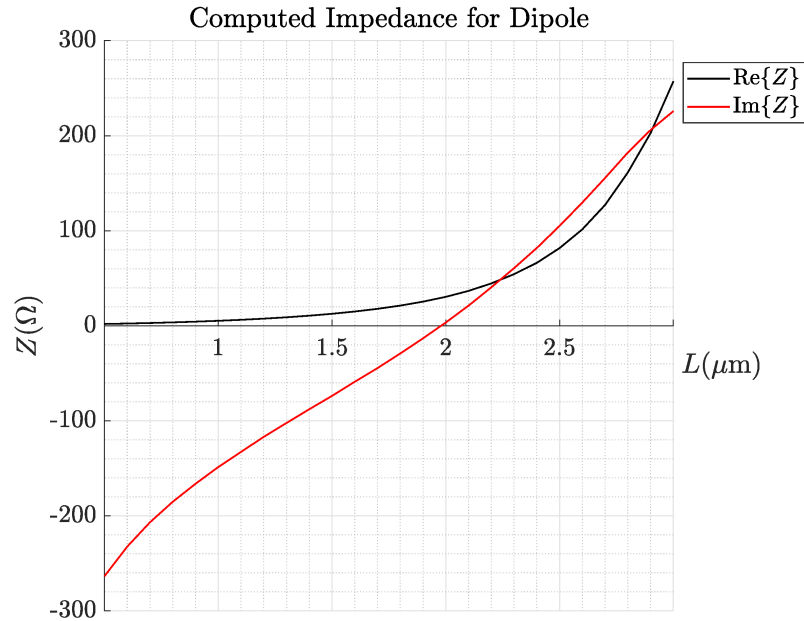
Figure 5.13: Computed input impedance for a dipole antenna operating at 28.3 THz as a function of the dipole length L. Shown in black is the antenna resistance (real part of the impedance) and in red the reactance (imaginary part of the impedance).

Once the dipole design has been determined, next the CPS has to be designed. The CPS has to be long enough to observe the propagating waves along the lines but not too long to avoid complete decay of the current waves. To pick the optimal length for the CPS, the designed dipole is coupled to two parallel transmission lines that make the CPS. The length of the CPS is a free parameter to vary in the simulation, the width of each line is 220 nm, they are separated by a 110 nm gap and the thickness of both lines is 100 nm. In this simulation, the purpose is not to measure the impedance of the antenna, instead it is to analyze the distribution of the electric field along the CPS as a function of the CPS length. The lumped port element does not provide analysis of the fields. So the simulation is configured without the lumped port, but a radiation boundary condition is added. This boundary condition sets up an incident electromagnetic wave incident into the simulation domain, and then the fields in the volume are solved. In order to replicate the s-SNOM experimental setup, the incident wave is specified as a plane wave, with a frequency of 28.3 THz, linearly polarized

along the direction of the dipole (x-axis) and incident at a 60° angle. The length L_c of the CPS is varied from 2 μm to 6μm in steps of 200 nm, and for each length the fractional power coupling for each structure is computed. This is chosen as a metric because the goal of the design is to find a dipole-CPS system that maximizes the amount of energy coupled into the structure. Fig. 5.14 shows a plot of the fractional power coupling as a function of the CPS length. This simulation shows a local maximum of coupling that occurs at $L_{\text{cps}} = 4.8$ μm, so this was the length used in the fabricated devices.
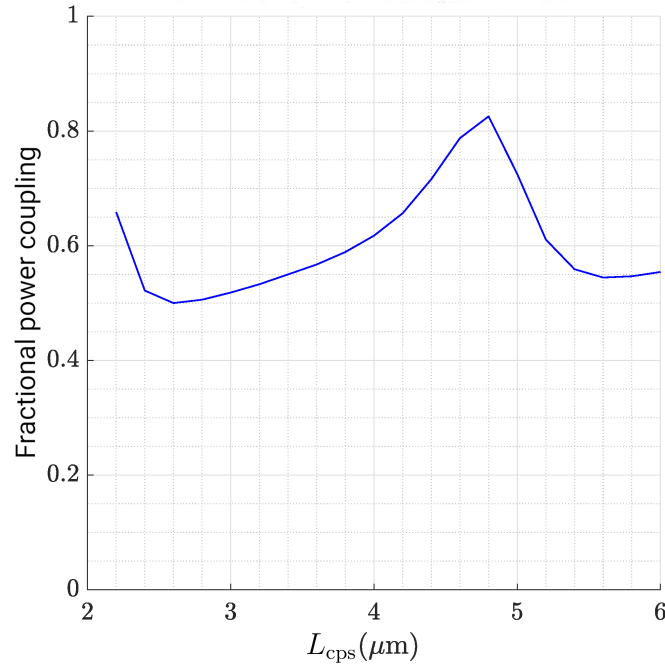
Figure 5.14: Computed fractional power coupling for the dipole-coupled CPS structure as a function of the CPS length L_{cps}.

The study of the near-field distribution on the dipole-coupled CPS can be achieved by extracting the magnitude of the z-component of the electric field ($|E_z|$) from the simulation at a plane 20 nm above the antenna. The reason for this particular choice of the $|E_z|$ field is because this is the component that the s-SNOM measures. Fig. 5.15 shows the simulated fields for the dipole-coupled CPS with a length of the transmission line of $L_{\text{cps}} = 4.8$ μm. The incident electromagnetic wave propagates

along the y-axis and is polarized along the x-axis. The results show the magnitude of the field is maximum at the ends of the dipole, which is characteristic of a resonant dipole [50, 51]. Most importantly, the magnitude of the field exhibits two maxima and two minima along the CPS, which is enough for subsequent analysis of the structure.
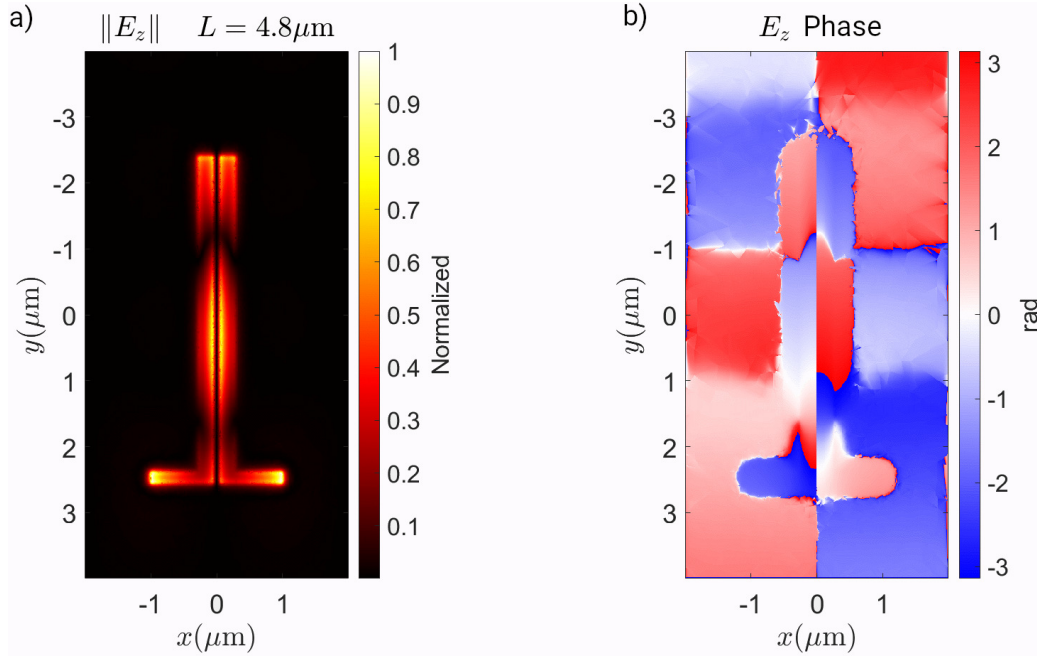
Figure 5.15: Computed electric field (z-component) above the dipole-coupled CPS. a) shows the modulus and b) the phase.

Since extraction of impedance of the antenna under test from the measured data depends on the impedance of the CPS, this has to be characterized. Also the impedance of the CPS can be determined by considering two structures: first the dipole-coupled CPS antenna terminated in an open circuit, and second terminated in a short circuit. The open-circuit termination is located at the opposite end of the CPS from the dipole and is left unconnected, while for the short-circuit the end is shorted by a metallic strip with a width of 150 nm. A diagram of these designs is shown in Fig. 5.16.
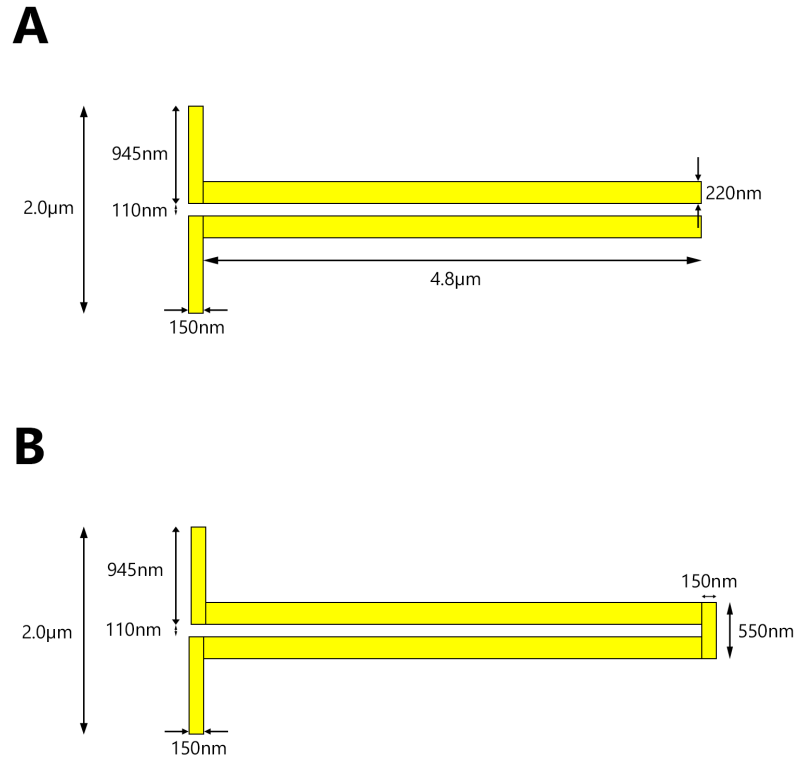
Figure 5.16: Design for A) the dipole-coupled CPS antenna terminated in an open circuit and B) the dipole-coupled CPS terminated in a short circuit.

5.2.1.4   Summary of Designs

Based on the simulations outlined in this section, designs for the antennas to test can be specified. Nine antennas in total are considered: six for modified folded dipoles, and three for t-match. The modified folded dipoles are labeled as antennas C, D, F, G, H, and I, whose dimensions are specified in Table 5.3. The t-match networks are labeled as antennas J, K, and L, and their dimensions are specified in Table 5.4. Each of these antenna designs are the load for a dipole-coupled CPS as shown in Fig. 5.17.

Table 5.3: Antenna dimensions for the fabricated modified folded dipole antennas.

Design	L (μm)	d (nm)	G (μm)
C	2.25	550	0.450
D	2.25	550	0.500
F	2.50	450	0.650
G	2.50	550	1.670
H	2.75	350	1.350
I	2.75	350	1.000

Table 5.4: Antenna dimensions for the fabricated t-match network antennas.

Design	L (μm)	L_t (μm)
J	3.00	2.80
K	3.00	2.78
L	3.25	2.70

a)

945nm

2.0µm   110nm

4.8µm

150nm

w

G   L

d

w

b)

945nm

2.0µm   110nm

4.8µm

150nm

L_t L

w

s

w
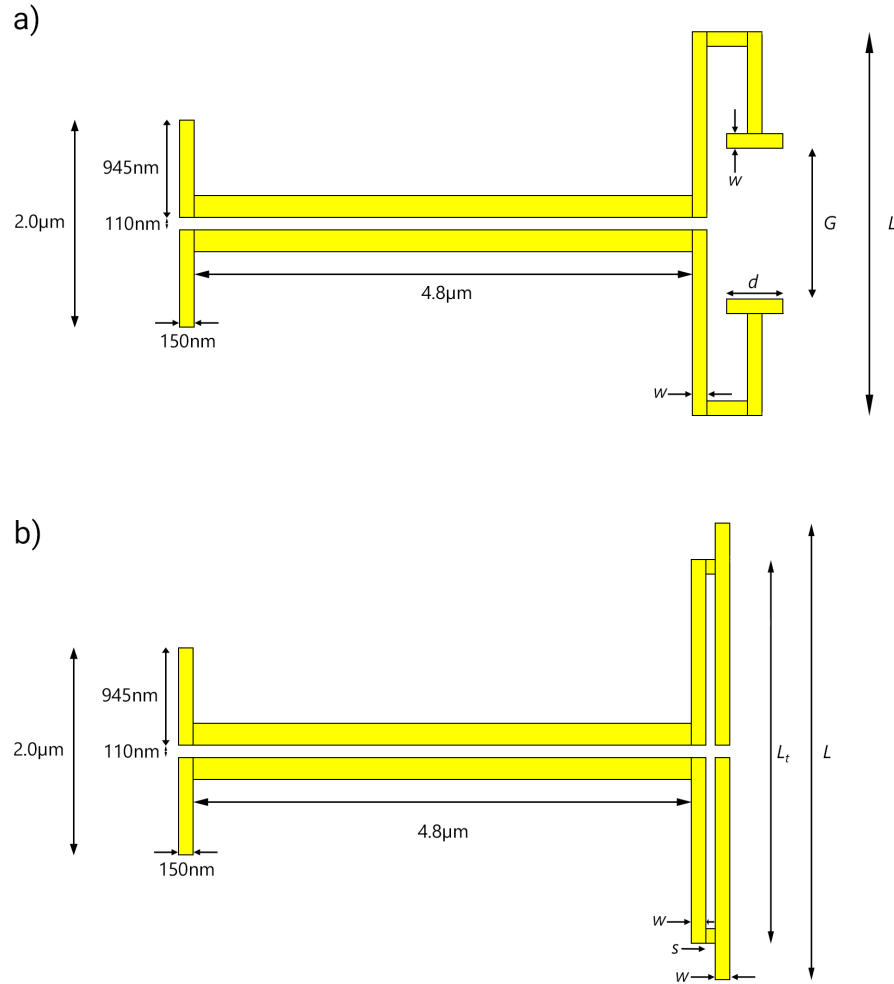
Figure 5.17: a) Design for the modified folded dipole antenna as the load for the dipole-coupled CPS. $w = 150$ nm is the antenna width and other parameters are given according to Table 5.3. b) Design for the t-match antenna as the load for the dipole-coupled CPS. $w = 150$ nm is the antenna width, $s = 100$ nm is the separation and other parameters are given according to Table 5.4.

5.2.2   Antenna Fabrication

The procedure followed for the fabrication of the antennas starts with a high resistivity silicon (Si) wafer (3-6 kΩ·cm). The wafer is then plasma cleaned and a 170-nm thick layer of Cr is e-beam evaporated to make the ground plane. Next, to make the substrate a 1 μm thick layer of ZnS is thermally evaporated (BOC Edwards Auto 306). To fabricate the antennas, standard procedure of electron-beam lithography (EBL) is used. First, a 300-nm thick layer of polymethyl methacrylate (PMMA) is

spin coated at 1750 rpm for 60 seconds and then baked on a hot plate at 180°C for 90 seconds. The antennas are patterned using the Raith 150 e-beam lithography system at a dose of 140 μC/cm^2, e-beam current of 19 nA, and 10kV acceleration voltage. The resist is then developed in a 3:1 solution of MIBK:IPA for 60 seconds, rinsed with IPA and then blow-dried with a nitrogen gun.

The antennas were fabricated using e-beam evaporation (Kurt J Lesker PVD 75). A 100-nm-thick layer of Au is deposited over a 3-nm layer of Ti which serves as an adhesion layer between the Au and the ZnS substrate. Lift-off of the unexposed resist was done in a bath of Remover PG for two days followed by ultrasonic agitation for 15 seconds. After rinsing the sample and blow drying it, the antennas are finished.

The overall fabrication procedure can be seen as a ten-step process that is schematically depicted in Fig. 5.18, showing the profile of the sample at each step. These ten steps are a) wafer cleaning, followed by deposition of the b) ground plane, c) substrate , and d) resist. Followed by e) e-beam exposure and f) development. Lastly the antenna is made at the steps g) metallization and h) lift-off.
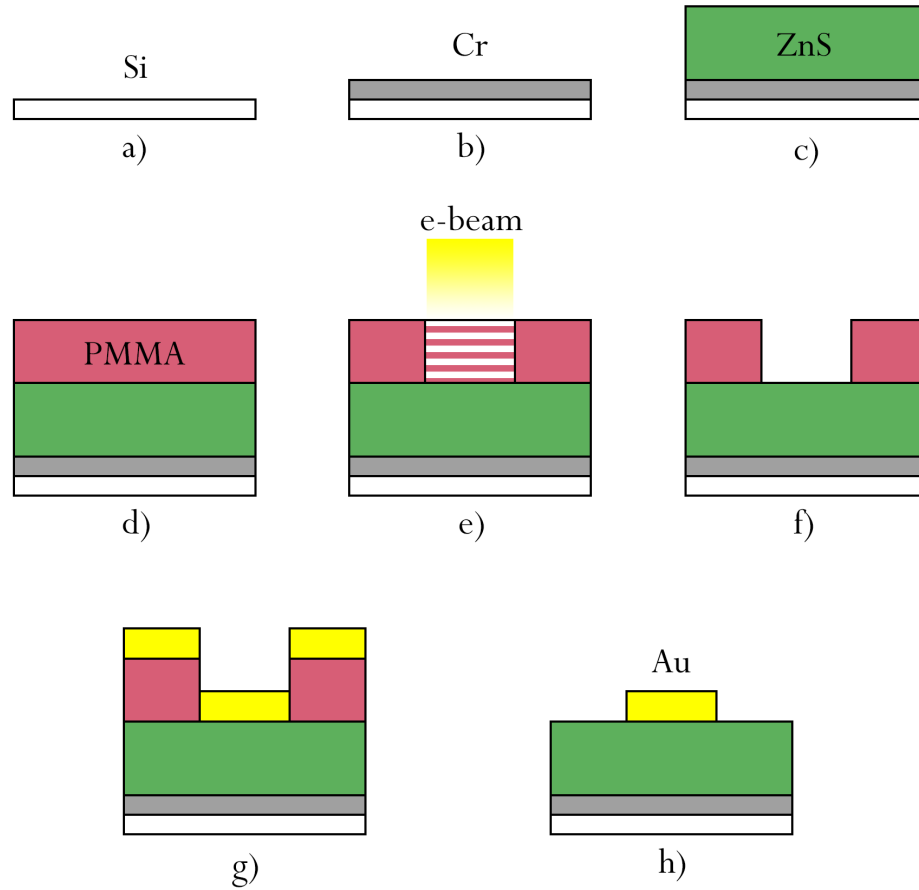
Figure 5.18: Step by step diagram of the micro fabrication procedure. a) Starting cleaned Si wafer. b) Evaporation of a 150 nm thick Cr layer. c) Evaporation of a 1 μm thick ZnS layer. d) Spin coating of PMMA resist. e) E-beam patterning of the antennas. f) Resist development. g) Metallization of 100 nm thick Au layer. h) Resist lift-off (dimensions of the layers are not to scale).

The antennas were fabricated in a 5×5 grid, with a 20 μm spacing between each antenna to avoid mutual coupling effects. Fig. 5.19 shows a micrograph of the fabricated antennas of one grid, this in particular contains five copies of antennas F, G, H, I and J. Each antenna design is coupled to the same dipole-CPS system. Micrographs with higher magnification of the modified folded dipole antenna and the t-match network are shown in Figs. 5.20 and 5.21, respectively.
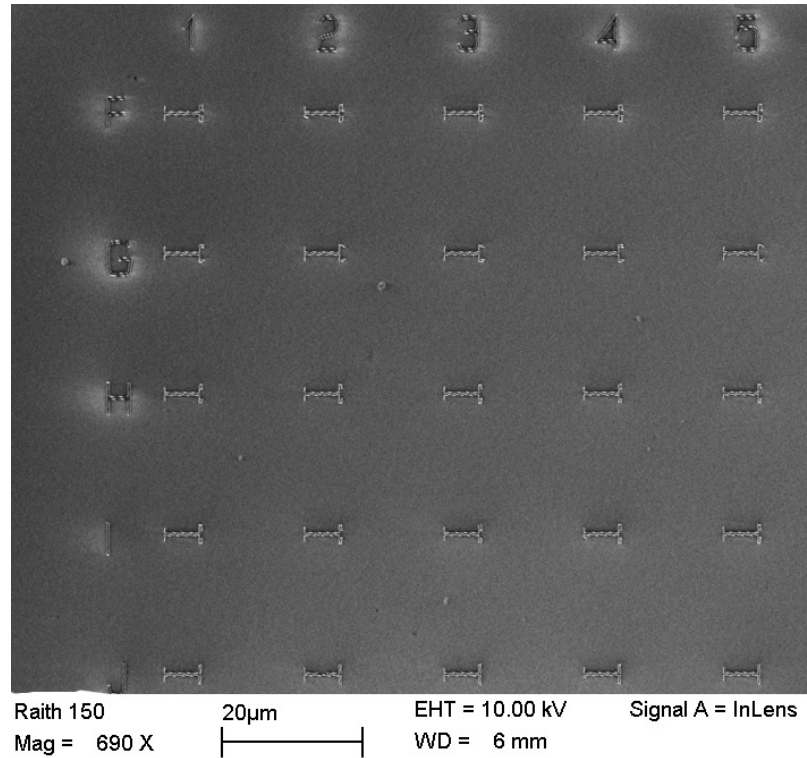
Figure 5.19: Scanning electron microscope image of a single grid of the fabricated antennas. Each row is a series of five copies of the antenna designs F, G, H, I and J.
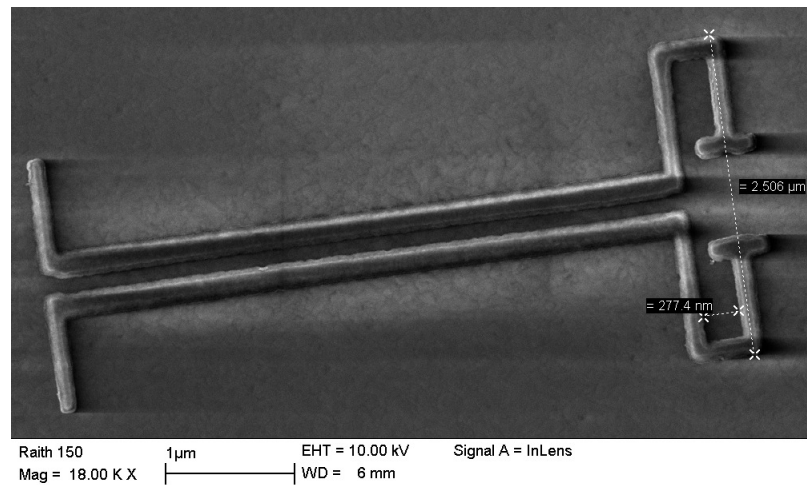
Figure 5.20: Scanning electron microscope image of the fabricated modified folded dipole design F coupled to a dipole-CPS coupling. Dotted lines indicate the length L and the internal width of the folded dipole.
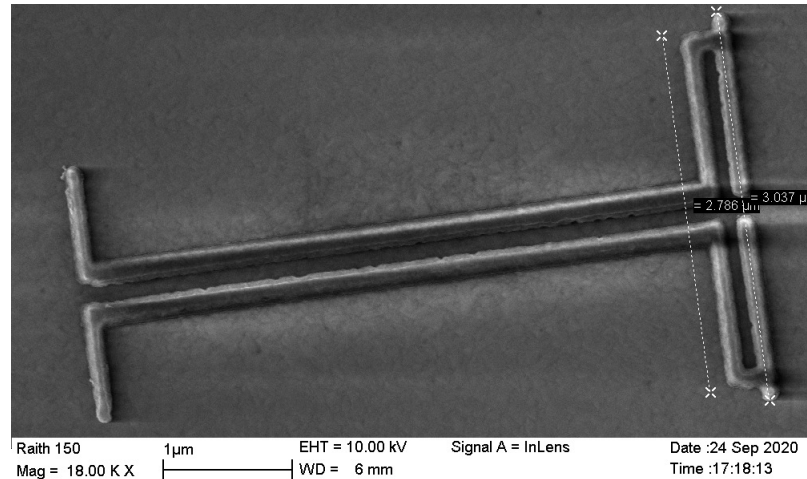
Figure 5.21: Scanning electron microscope image of the fabricated t-match design J coupled to a dipole-CPS coupling. Dotted lines indicate the length L and L_t.

5.2.3   Near-field Measurements and Analysis

These sections present the experimental data and the subsequent analysis to characterize the fabricated antennas. Near-field measurements of each antenna were performed using the s-SNOM technique. First the dipole-coupled CPS with open- and short-circuit loadings are analyzed in order to characterize the CPS. Once the impedance of the CPS is determined, the modified folded dipole and t-match antennas are characterized.

5.2.3.1   CPS Characterization

Given the experimental conditions, the incident wave illuminates the dipole-coupled CPS. As a consequence, fields will couple in at the dipole launching a propagating wave with amplitude E_0 along the CPS. This forward propagating wave will reach the opposite end of the CPS and it will be reflected as a backward propagating wave. The amplitude of this new wave is $\Gamma_o E_0$, where Γ_o is the reflection coefficient at the end of the transmission line. For the open-circuit termination case, the reflection coefficient is $\Gamma_o = 1$, meaning that the amplitude of the wave is unchanged. Since there is no amplitude loss on reflection, then the backwards propagating wave is expected to

reach the dipole. This wave will be reflected at the dipole, with a reflection coefficient Γ_D. Given the wave attenuation over the length, further reflections are negligible [52]. So overall there are three propagating waves along the CPS. The impedance of the CPS is giving by

$$Z_{\text{cps}} = \frac{1 - \Gamma_D}{1 + \Gamma_D} Z_D, \tag{5.3}$$

where $Z_D = 30.48 \ \Omega$ is the impedance of the dipole. Therefore, the CPS will be characterized if the reflection coefficient Γ_D is determined. To characterize the CPS, recall the three propagating waves on the CPS mentioned above. If the CPS is assumed to lie along the y-axis, the forward propagation occurs in the positive y direction and the dipole is at the origin, then the superposition of these waves generates a standing wave along the CPS, which is described by

$$E(y) = E_0 \left[e^{-(\alpha - i\beta)y} + \Gamma_o \left(e^{(\alpha - i\beta)(y - 2L_{\text{cps}})} + \Gamma_D e^{-(\alpha - i\beta)(y + 2L_{\text{cps}})} \right) \right], \tag{5.4}$$

where α and β are the attenuation and propagation constants, respectively, and $L_{\text{cps}} = 4.8 \ \mu\text{m}$ is the length of the CPS.

Eq. (5.4) describes the standing wave along the CPS for the open-circuit design introduced in subsection 5.2.1.3. Hence, by measuring the electromagnetic field along the CPS, the reflection coefficient Γ_D can be determined by fitting the experimental data to Eq. (5.4). For the case of the short-circuit design, since the size of the shorting is smaller than the dipole, field coupling from the incident wave and the current waves generated at the shorting is negligible compared to the one originated at the dipole. Therefore the standing wave along the CPS for the short-circuit case is also given by Eq. (5.4).

The standing-wave parameters are determined by a non-linear fitting algorithm that minimizes the sum-squared error to the measured near-field data. Implicit in this analysis is the assumption that the s-SNOM measured signal is equal to the

magnitude of the fields on the antenna under test. These two fields are proportional to each other. For our purposes the absolute magnitude of the fields are not of interest. The interest lies on the relative behavior of these fields, which determines the reflection coefficients.
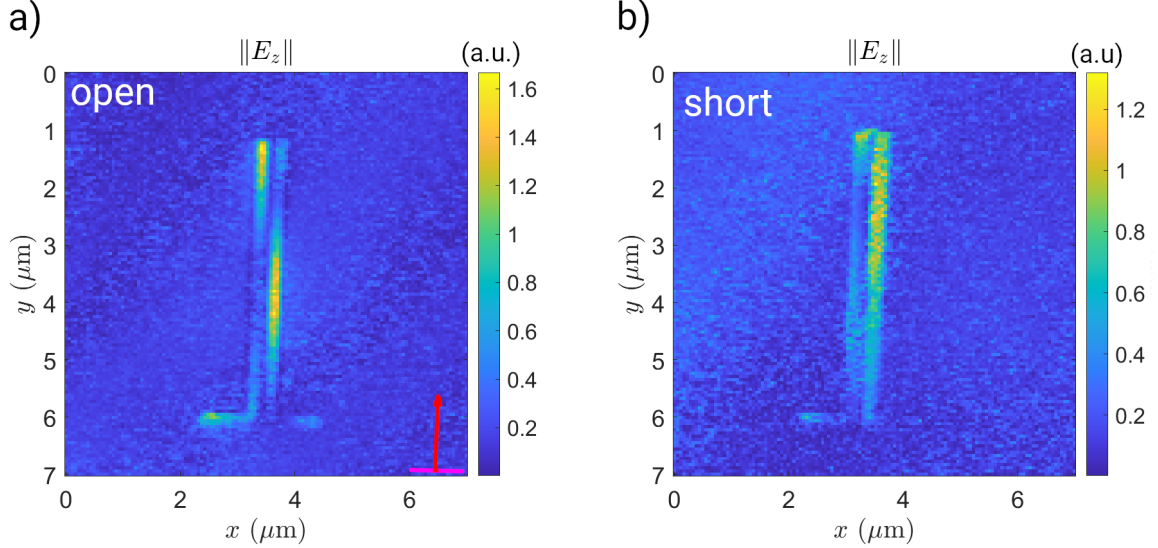
Figure 5.22: Measured s-SNOM signal for the dipole-coupled CPS antennas with an a) open-circuit load and b) short-circuit load. The red arrow and purple line in a) represent the projection of the propagation vector into the xy plane and the polarization of the incident wave, respectively.

The collected near-field maps for the open-circuit and short-circuit terminations are shown in Fig. 5.22. In these maps, the incoming radiation is incident from the bottom of the frame and propagates upwards, and the wave is linearly polarized along the x-axis. The data to consider for the fit is the collected near-field along the CPS for each antenna structure. Notice that the CPS is composed of two conducting lines. Therefore two independent fits are done, the first one to the left conductor and the second one to the right conductor. It is worth noticing that the fields on the conductors have the same magnitude but there is a phase difference of 180° therefore a π phase term is added to Eq. (5.4) when fitting the right conductor [49]. Additionally, since each conductor has a finite width, the magnitude of the near field is averaged across this width, which is then fitted to Eq. (5.4). The resultant fits to the standing
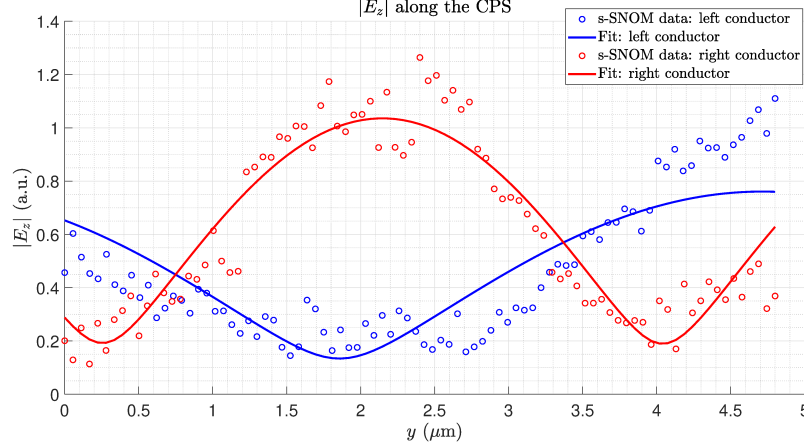
Figure 5.23: Non-linear least squares fit of the near-field for the dipole-coupled CPS antennas with an open-circuit load, along the left and right conductors of the CPS drawn in blue and red, respectively. Dots represent the experimental data and the continuous line represents the best fit for the respective conductor.

waves along the CPS in the open-circuit case are shown in Fig. 5.23.

In order to obtain a better estimate of the reflection coefficient, five s-SNOM scans are performed for both the dipole-coupled CPS antenna with open- and short-circuit ends. For each scan, the standing waves along the CPS are fitted to Eq. (5.4) and the reflection coefficient is obtained. These coefficients are averaged over the five measurements and this average is used to calculate the impedance of the CPS using Eq. (5.3). The resultant reflection coefficients and impedances from this analysis are specified in Table 5.5.

Table 5.5: Reflection coefficients and calculated impedance for the dipole-coupled CPS.

Design	$|\Gamma_D|$	Z_{cps} (Ω)
Open-circuit	0.05 ± 0.01	27.8 ± 0.8
Short-circuit	0.06 ± 0.01	27.0 ± 0.7

Given the CPS in the open- and short-circuit cases are identical, the impedance for both cases is expected to be the same. The impedance we use for subsequent analysis is the average between both cases: $Z_{\mathrm{cps}} = 27.4 \pm 1.0$ Ω. Once the CPS has

been characterized, these results can be used to characterize the designed antennas: the modified folded dipole and t-match.

5.2.3.2   Modified Folded Dipole

The collected near-field maps for the modified folded dipoles structures are shown in Fig. 5.24.
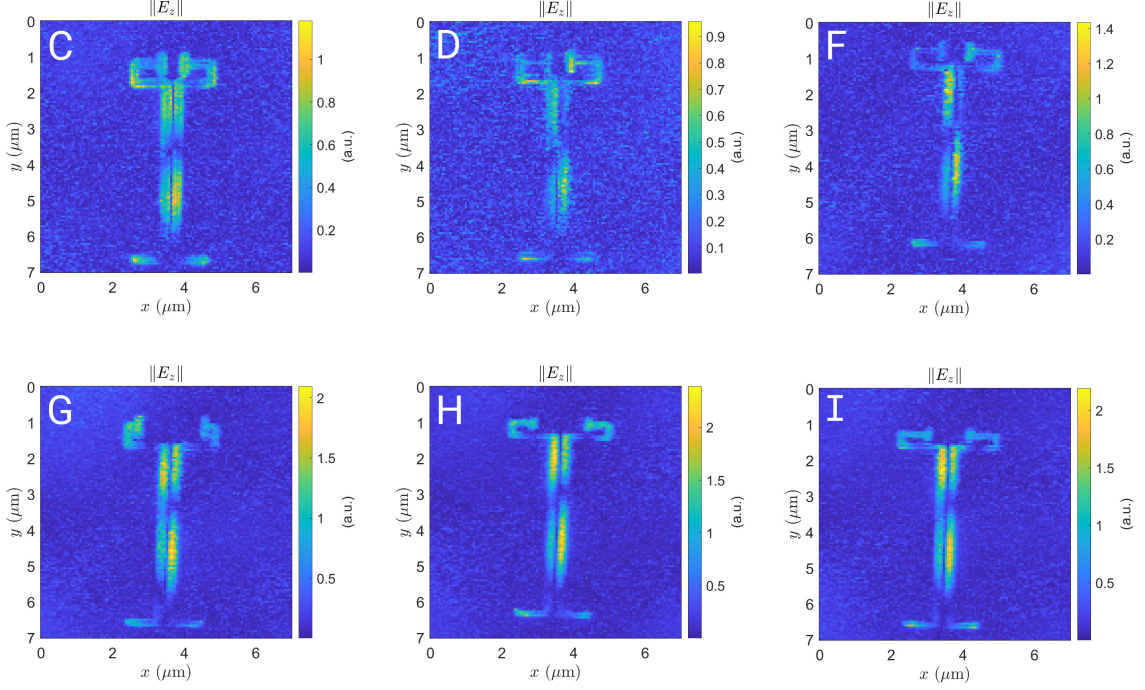
Figure 5.24: Measured s-SNOM signal for the dipole-CPS-modified folded dipole antenna system. From top to bottom and from left to right, the maps show the near-field distribution for designs C, D, F, G, H and I. The red arrow and purple line in the top-left map represent the projection of the propagation vector into the xy plane and the polarization of the incident wave, respectively.

Given the experimental conditions, the incident wave illuminates the dipole-CPS-AUT system. As a consequence, fields will couple at the dipole launching a propagating wave along the CPS. This forward propagating wave will reach the AUT (either the modified folded dipole or t-match antenna) and then it will be reflected. After reflection, the wave will travel in the opposite direction. In a similar fashion, fields will couple at the AUT, launching a propagating wave in the backwards direction along the CPS towards the dipole. At the dipole, this wave will be reflected and its

reflection will propagate in the forward direction. Therefore along the CPS there are four propagating waves that will superimpose and create a standing wave. If the CPS lies along the y-axis and the origin of coordinates is at the dipole, then the AUT will be located at the end of the CPS, i.e. $y = L_{\mathrm{cps}} = 4.8~\mu$m. So the standing wave along the CPS can be described by

$$E_z(y) = E_D \left[e^{-(\alpha-i\beta)y} + \Gamma_L e^{(\alpha-i\beta)(y-2L_{\mathrm{cps}})} \right] + E_L \left[e^{(\alpha-i\beta)(y-L_{\mathrm{cps}})} + \Gamma_D e^{-(\alpha-i\beta)(y+L_{\mathrm{cps}})} \right],$$

$$(5.5)$$

where E_D and E_L are the field amplitudes of the propagating waves originating at the dipole and the load, respectively. The attenuation and propagation constants are α and β, respectively. And Γ_D and Γ_L are the reflection coefficients at the dipole and load, respectively. In this case, the load is the AUT.

The data to consider for the fit is the collected near field along the CPS for each antenna structure. Since the CPS is composed of two conductors, two independent fits are done, the first one to the left conductor and the second one to the right conductor. Since each conductor has a finite width, the magnitude of the near field is averaged across this width and then fitted to Eq. (5.5). As an example, the resultant fits to the standing waves along the CPS for design C are shown in Fig. 5.25. In principle, the conductors in the CPS are identical and both dipole antenna and the modified folded antenna are symmetrical, so one should expect the standing waves along both conductors to be identical. Looking at the experimental data, the two standing waves are not identical, however the local maxima and minima occur approximately at the same locations. Differences in the amplitudes of the fields can be attributed to height variances between the antenna plane and the AFM tip in the s-SNOM setup. Since near-field measurements are enhanced when the tip is in close proximity to the antenna, any small tilt in the antenna plane will impact the measured field strength (appendix C includes a detailed discussion on the origin of this

tilt). However, these differences in the amplitudes are unimportant to the relative relation of the fields that ultimately determine the reflection coefficients. In the particular example of the standing waves along the antenna design C, the non-linear fit for the left conductor shows that the wave parameters are: $\alpha = 0.13 \pm 0.05$ $\mu\mathrm{m}^{-1}$, $\beta = 1.32 \pm 0.06$ rad/μm and $\Gamma_L = 0.93 \pm 0.06$. While for the right conductor the parameters are: $\alpha = 0.10 \pm 0.05$ $\mu\mathrm{m}^{-1}$, $\beta = 1.48 \pm 0.06$ rad/μm and $\Gamma_L = 0.98 \pm 0.06$.
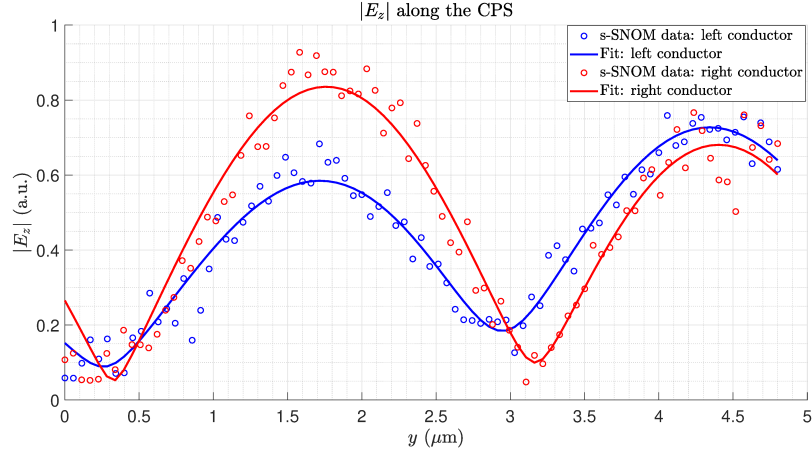
Figure 5.25: Non-linear least squares fit of the near-field for antenna design C, along the left and right conductors of the CPS drawn in blue and red, respectively. Dots represent the experimental data and the continuous line represent the best fit for the respective conductor.

Results from the fits above suggest that the standing waves along the left and right conductors are in agreement, which is expected from the symmetry of the structure. So to obtain a better estimation of the standing wave parameters, in particular the reflection coefficient at the load Γ_L, five s-SNOM scans are taken of each antenna structure design. For each scan, the field along the conductors is fitted to Eq. (5.5) and the reflection coefficient Γ_L is obtained. Then the reflection coefficient that characterizes each antenna design is determined from the average over all the Γ_L obtained from the fits. Once the respective reflection coefficient has been determined, the antenna impedance be can calculated using Eq. (1.4). The measured reflection coefficients for each antenna and the respective calculated impedances are listed in

Table 5.6.

Table 5.6: Reflection coefficients and calculated impedance for the modified folded dipoles structures determined experimentally.

Design	$|\Gamma_L|$	Z (kΩ)
C	0.968 ± 0.024	1.71 ± 0.08
D	0.968 ± 0.022	1.70 ± 0.08
F	0.964 ± 0.026	1.51 ± 0.07
G	0.952 ± 0.057	1.11 ± 0.08
H	0.954 ± 0.045	1.15 ± 0.07
I	0.960 ± 0.028	1.33 ± 0.06

Experimental results suggest that the implementation of the modified folded dipole design with the adequate dimensions can achieve an antenna with impedance above 1 kΩ at infrared frequencies. The antenna impedance ranges from 1.11 kΩ, for design G, to 1.71 kΩ, for design C. This confirms the close relationship between the choice of antenna dimensions and the impedance. To study this relationship further, the antenna impedance is plotted as a function of the ratio of the antenna length L to the antenna gap G. This plot is shown in Fig. 5.27. For comparison, the expected impedance from numerical simulations is shown in this plot as well. For this set of simulations, the dimensions of the fabricated antennas were measured from the scanning electron-microscope micrographs and the impedance of each design was computed. As seen in the plot, as the L/G ratio increases the antenna impedance increases. This relationship can be observed for both the numerical predictions and the experimental results. Although the impedance obtained from the experiment and the simulations are in the same order of magnitude, there is an overall offset for which the impedance of the fabricated antennas is greater. This offset can be attributed to two factors. The first one is due to the fact that in the simulations the antennas are

modeled as blocks with all sides perpendicular to each other. However close inspection of the fabricated antennas (see Fig. 5.26) shows the top end of the antenna (at the antenna-air interface) does not have the same width as the bottom end (at the antenna-substrate interface). The bottom end is wider than at the top, so the profile of the antenna resembles a trapezoid and not a rectangle, causing the difference in the impedance results. The second factor lies on the surfaces of the structures in the simulations that, for simplicity of the modeled, are assumed to be flat and smooth. However the metallization and lift-off process does not yield into a smooth surface for the antennas. This resultant surface roughness in the fabricated structures increases both the attenuation of the wave across the CPS as well as the load antenna impedance [53, 54].
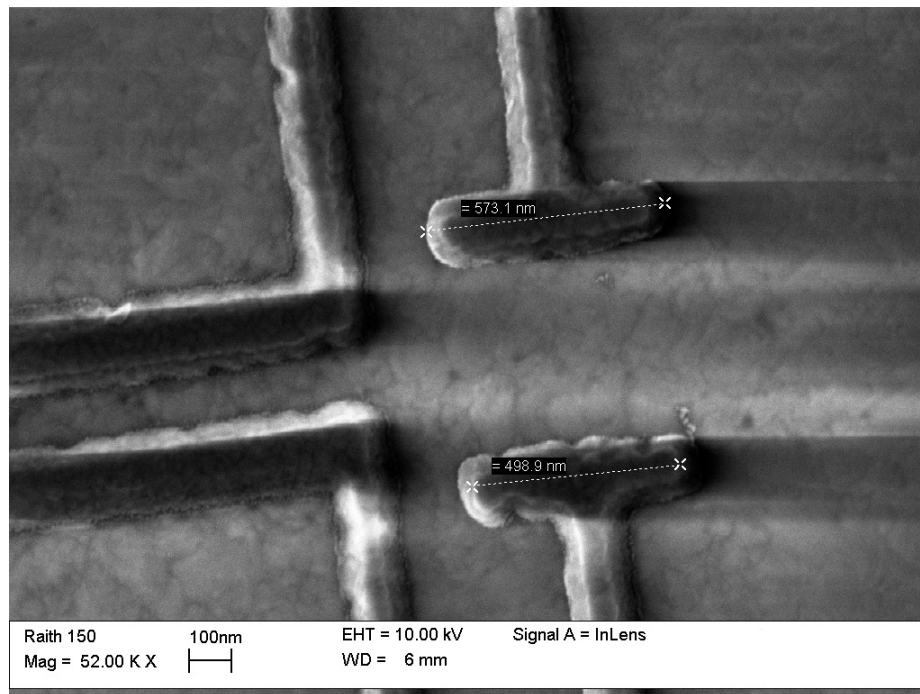
Figure 5.26: Micrograph of the modified folded dipole with a 52K magnification. Dotted lines indicate the different sizes of the stubs that make the antenna.
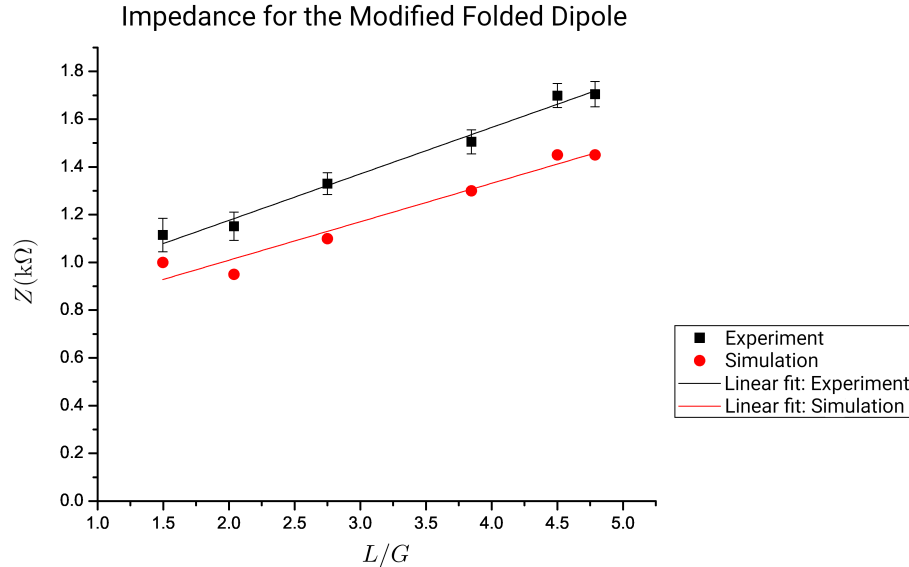
Figure 5.27: Impedance as a function of the ratio L/G of the modified folded dipole. Shown in black are the impedances determined experimentally and the linear fit that best fits the data. Shown in red are the impedance predictions from the simulations.

5.2.3.3   T-Match

In a similar fashion as in the previous section, near-field maps for the dipole-coupled t-match were collected using s-SNOM and the results are shown in Fig. 5.28. The illumination conditions for the t-match structure are the same as the conditions for the modified folded dipole. This means the incident electromagnetic wave couples into the two antennas at the ends at the CPS and propagating waves along the CPS create a standing wave along the CPS as in Eq. (5.5). Then the impedance of the antenna design can be obtained from the measured magnitude of the near-field along the CPS via a non-linear least squares fit. Similar as in the case of the modified folded dipoles, five near-field s-SNOM scans were used to find the reflection coefficient and the impedance for each of the structures. These results are specified in Table 5.7. The tested antennas have an impedance in the order of 0.80 kΩ, impedance that is significantly larger than the impedance of a resonant dipole antenna at this frequencies, but not as large as the impedance for the modified folded dipoles in the previous section. Hence this design could offer impedance matching to loads with

resistance in this same order of magnitude.
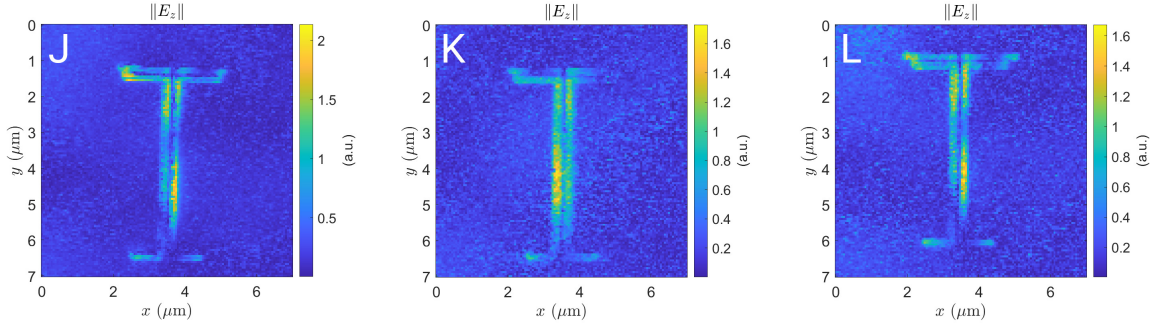
Figure 5.28: Measured s-SNOM signal for the dipole-CPS-T-match antenna system. From left to right the maps show the near-field distribution for designs J, K and L. The red arrow and purple line in the top-left map represent the projection of the propagation vector into the xy plane and the polarization of the incident wave, respectively.

Table 5.7: Reflection coefficients and calculated impedance for the dipole-coupled t-match structures determined experimentally.

Design	$|\Gamma_L|$	Z (kΩ)
C	0.934 ± 0.062	0.80 ± 0.06
D	0.933 ± 0.083	0.80 ± 0.08
F	0.932 ± 0.079	0.78 ± 0.07

CHAPTER 6: CONCLUSIONS AND FUTURE WORK

Characteristics of infrared antennas and resonant structures were studied in order to improve existing measurement methods and study novel antenna designs that improve antenna parameters such as localized hot spots, bandwidth and impedance matching.

In Chapter 3 an improvement of infrared scattering-scanning near-field microscopy was introduced. In traditional heterodyne operation of s-SNOM multiple scans are required in order to retrieve the magnitude and the phase of the near-field of a sample. Pseudoheterodyne operation reduces the number of scans to a single one, however ambiguity on the phase is present. This ambiguity can be avoided when collecting the appropriate signals and postprocessing them so the signal sign is recovered and be accounted in the phase calculation. After implementing these improvements in the s-SNOM signal analysis, experimental results for the retrieved phase are in agreement with the expected phase computed from numerical solutions.

In Chapter 4 a novel infrared bow-tie antenna is introduced and studied using the improved pseudoheterodyne scheme for s-SNOM. The design of this bow-tie antenna is inspired on the classical design, but in this structure the area that constitutes the antenna has been discretized. The discretization is done by filling the antenna area with finite circular elements of different sizes. Computational simulations suggest that this discretization enhances antenna parameters such as bandwidth and hot spot density over the antenna area. The discrete bow-tie antenna was fabricated and its behavior was studied using s-SNOM. Experimental results confirmed the enhancement of hot-spot locations across the metallic structure under different polarization conditions. These features are of particular interest for surface enhanced Raman spectroscopy, biosensing or plasmon generation applications where field enhancement

is critical. The results from this study represent the validation of an hypothesis that opens a new door for exploration. For instance, the enhancement of antenna parameters that the discrete bow-tie antenna exhibits represents an opportunity to explore alternative discretization methods. These include, but are not limited to, the study of the impact different discrete elements, not only circular, and algorithms can have on the antenna parameters. Also the study of alternative antenna designs, such as patch or spiral antennas, and their behavior as discretized designs.

Chapter 5 is dedicated to the study of two main approaches of impedance matching techniques. The first technique involves an antenna-coupled metal-oxide-metal diode under DC bias. Previous work suggest that MOM diodes coupled to antennas are suitable for infrared detectors. However for this detector to be efficient, the impedance of its elements, namely the antenna and the diode, must be matched. To achieve matching, a bias DC voltage is applied across the diode in order to tune its resistance. Experimental measurements conducted with s-SNOM sampled the near-field across the antenna-coupled diode under changing bias voltages. Results suggest the bias impacts the near-field distribution in an incremental manner, which is a response of the fields to the changing resistance of the diode due to the bias. This observation may be a promising avenue for active impedance tuning that can be explored in future work.

The second impedance matching technique involves the development of novel antennas that possess an impedance high enough so they could be matched with high-impedance diodes for infrared sensing purposes. Two antenna designs were introduced: first the modified folded dipole and second the dipole-coupled t-match. Numerical simulations suggest that by picking the appropriate antenna dimensions, these antennas are resonant for infrared frequencies and their resistance is on the order of $1 \text{ k}\Omega$. Based on these results, modified folded dipole antennas and dipole-coupled t-match were fabricated. Antenna impedance of these fabricated structures was mea-

sured using s-SNOM. In this approach, the superposition of propagating waves along the coplanar strip line allows the determination of the reflection coefficient at the antennas under test, which allows the measurement of the antenna impedance. Resultant impedances are in the order of 1 kΩ, proving that this antenna designs can achieve high resistance and this resistance can be tuned by selecting the suitable combination of antenna dimensions. The possibility of finding additional designs with alternative geometries exists, and it would be worth exploring in future work, with the goal of achieving higher antenna resistance. The subsequent steps for future research would include the implementation of these high impedance antennas coupled to a infrared detector, such as a metal-oxide-metal diode, to verify the enhanced sensitivity obtained by improved impedance match.

REFERENCES

[1] P. Aughton, *The Story of Astronomy* (Quercus Publishing, 2011).

[2] E. L. Dereniak and G. D. Boreman, *Infrared Detectors and Systems*, Wiley Series in Pure and Applied Optics (Wiley, 1996).

[3] A. Rogalski, *Infrared Detectors* (CRC Press, 2010).

[4] L. M. Matarrese and K. M. Evenson, "Improved coupling to infrared whisker diodes by use of antenna theory," Applied Physics Letters **17**(1), 8–10 (1970).

[5] B. Twu and S. E. Schwarz, "Properties of infrared cat whisker antennas near 10.6 μ," Applied Physics Letters **26**(12), 672–675 (1975).

[6] C. A. Balanis, "Antenna Theory : A Review," Proceedings of the IEEE **80**(1), 7–23 (1992).

[7] D. M. Pozar, *Microwave Engineering* (Wiley, 2011).

[8] P. Bharadwaj, B. Deutsch, and L. Novotny, "Optical Antennas," Advances in Optics and Photonics **1**(3), 438 (2009).

[9] G. D. Boreman and J. Alda, *Infrared Antennas and Resonant Structures* (SPIE, Bellingham, 2017).

[10] S. E. Schwarz and B. T. Ulrich, "Antenna coupled infrared detectors," Journal of Applied Physics **48**(5), 1870–1873 (1977).

[11] P. Esfandiari, G. Bernstein, P. Fay, W. Porod, B. Rakos, A. Zarandy, B. Berland, L. Boloni, G. Boreman, B. Lail, B. Monacelli, and A. Weeks, "Tunable antenna-coupled metal-oxide-metal (MOM) uncooled IR detector," in *Infrared Technology and Applications XXXI*, B. F. Andresen and G. F. Fulop, eds., vol. 5783, p. 470 (2005).

[12] T. Ishi, J. Fujikata, K. Marita, T. Baba, and K. Ohashi, "Si nano-photodiode with a surface plasmon antenna," Japanese Journal of Applied Physics, Part 2: Letters **44**(12-15) (2005).

[13] L. Tang, S. E. Kocabas, S. Latif, A. K. Okyay, D.-S. Ly-Gagnon, K. C. Saraswat, and D. A. B. Miller, "Nanometre-scale germanium photodetector enhanced by a near-infrared dipole antenna," Nature Photonics **2**(4), 226–229 (2008).

[14] J. A. Bean, A. Weeks, and G. D. Boreman, "Performance Optimization of Antenna-Coupled Al/AlO/Pt Tunnel Diode Infrared Detectors," IEEE Journal of Quantum Electronics **47**(1), 126–135 (2011).

[15] H. A. Atwater and A. Polman, "Plasmonics for improved photovoltaic devices," Nature Materials **9**(3), 205–213 (2010).

[16] L. Novotny and N. van Hulst, "Antennas for light," Nature Photonics **5**(2), 83–90 (2011). `1305.0033`.

[17] C. A. Balanis, *Antenna Theory: Analysis and Design*, no. v. 1 in Antenna Theory: Analysis and Design (John Wiley & Sons, 2005).

[18] R. L. Olmon, P. M. Krenz, A. C. Jones, G. D. Boreman, and M. B. Raschke, "Near-field imaging of optical antenna modes in the mid-infrared," Optics Express **16**(25), 20,295 (2008).

[19] R. Holm, *Electric Contacts*, 4th ed. (Springer Berlin Heidelberg, Berlin, Heidelberg, 1967).

[20] A. Alù and N. Engheta, "Input Impedance, Nanocircuit Loading, and Radiation Tuning of Optical Nanoantennas," Physical Review Letters **101**(4), 043,901 (2008). `0710.3411`.

[21] A. Alù and N. Engheta, "Hertzian plasmonic nanodimer as an efficient optical nanoantenna," Physical Review B - Condensed Matter and Materials Physics **78**(19), 1–6 (2008). `0807.1783`.

[22] J.-S. Huang, T. Feichtner, P. Biagioni, and B. Hecht, "Impedance matching and emission properties of optical antennas in a nanophotonic circuit," Nano Letters **9**(5), 1897–1902 (2008). `0811.2513`.

[23] M. Schnell, a. García-Etxarri, a. J. Huber, K. Crozier, J. Aizpurua, and R. Hillenbrand, "Controlling the near-field oscillations of loaded plasmonic nanoantennas," Nature Photonics **3**(April), 287–291 (2009).

[24] Y. Xu, E. Tucker, G. Boreman, M. B. Raschke, and B. A. Lail, "Optical Nanoantenna Input Impedance," ACS Photonics **3**(5), 881–885 (2016).

[25] L. Novotny, "Effective wavelength scaling for optical antennas," Physical Review Letters **98**(26), 1–4 (2007).

[26] J. L. Volakis, A. Chatterjee, L. C. Kempel, I. Antennas, and P. Society, *Finite Element Method Electromagnetics: Antennas, Microwave Circuits, and Scattering Applications*, IEEE Press Series on Electromagnetic Wave Theory (Wiley, 1998).

[27] H. Tompkins and E. A. Irene, *Handbook of Ellipsometry* (Elsevier Science, 2005).

[28] M. Fox, *Optical Properties of Solids*, Oxford Master Series in Physics (OUP Oxford, 2010).

[29] P. Rai-Choudhury and I. of Electrical Engineers, *Handbook of Microlithography, Micromachining, and Microfabrication: Microlithography*, Handbook of Microlithography, Micromachining, and Microfabrication (SPIE Optical Engineering Press, 1997).

[30] J. G. Goodberlet, J. T. Hastings, and H. I. Smith, "Performance of the Raith 150 electron-beam lithography system," Journal of Vacuum Science & Technology B: Microelectronics and Nanometer Structures **19**(6), 2499 (2001).

[31] K. S. Harsha, *Principles of Vapor Deposition of Thin Films* (Elsevier, 2006).

[32] R. Hillenbrand and F. Keilmann, "Complex optical constants on a subwavelength scale," Physical Review Letters **85**(14), 3029–3032 (2000).

[33] R. Hillenbrand, B. Knoll, and F. Keilmann, "Pure optical contrast in scattering-type scanning near-field microscopy," Journal of Microscopy **202**(1), 77–83 (2001).

[34] N. Ocelic, A. Huber, and R. Hillenbrand, "Pseudoheterodyne detection for background-free near-field spectroscopy," Applied Physics Letters **89**(10), 101,124 (2006).

[35] C. Moreno, J. Alda, E. Kinzel, and G. Boreman, "Phase imaging and detection in pseudo-heterodyne scattering scanning near-field optical microscopy measurements," Applied Optics **56**(4), 1037 (2017).

[36] J. M. López-Alonso, J. Alda, and E. Bernabéu, "Principal-component characterization of noise for infrared images," Applied Optics **41**(2), 320 (2002).

[37] C. Moreno, J. Méndez-Lozoya, G. González, F. J. González, and G. Boreman, "Near-field analysis of discrete bowtie plasmonic nanoantennas," Microwave and Optical Technology Letters **62**(2), 943–948 (2019).

[38] J. Mendez, G. González, A. Cuadrado, J. Alda, and F. González, "Discrete bowtie plasmonic nanoantenna," in *12th European Conference on Antennas and Propagation (EuCAP 2018)*, pp. 147 (4 pp.)–147 (4 pp.) (Institution of Engineering and Technology, 2018).

[39] A. Rogalski, "Infrared detectors: status and trends," Progress in Quantum Electronics **27**(2-3), 59–210 (2003).

[40] L. Becker, "Influence of IR sensor technology on the military and civil defense," Quantum Sensing and Nanophotonic Devices III **6127**(February 2006), 61,270S (2006).

[41] F. Gonzalez, B. Ilic, J. Alda, and G. Boreman, "Antenna-coupled infrared detectors for imaging applications," IEEE Journal of Selected Topics in Quantum Electronics **11**(1), 117–120 (2005).

[42] I. Baker, D. Owton, K. Trundle, P. Thorne, K. Storie, P. Oakley, and J. Copley, "Advanced infrared detectors for multimode active and passive imaging applications," in *Infrared Technology and Applications XXXIV*, B. F. Andresen, G. F. Fulop, and P. R. Norton, eds., vol. 6940, p. 69402L (2008).

[43] A. Rogalski, "Infrared detectors: an overview," Infrared Physics & Technology **43**(3-5), 187–210 (2002).

[44] A. Sanchez, C. F. Davis, K. C. Liu, and A. Javan, "The MOM tunneling diode: Theoretical estimate of its performance at microwave and infrared frequencies," Journal of Applied Physics **49**(10), 5270–5277 (1978).

[45] I. Codreanu, F. J. Gonzalez, and G. D. Boreman, "Detection mechanisms in microstrip dipole antenna-coupled infrared detectors," Infrared Physics & Technology **44**(3), 155–163 (2003).

[46] E. Tucker, J. D'Archangel, and G. Boreman, "Near- and far-field investigation of dark and bright higher order resonances in square loop elements at mid-infrared wavelengths," Optics Express **25**(5), 5594 (2017).

[47] J. D' Archangel, E. Tucker, E. Kinzel, E. A. Muller, H. A. Bechtel, M. C. Martin, M. B. Raschke, and G. Boreman, "Near- and far-field spectroscopic imaging investigation of resonant square-loop infrared metasurfaces," Optics Express **21**(14), 17,150 (2013).

[48] J. Ginn, D. Shelton, P. Krenz, B. Lail, and G. Boreman, "Altering infrared metamaterial performance through metal resonance damping," Journal of Applied Physics **105**(7), 074,304 (2009).

[49] P. M. Krenz, R. L. Olmon, B. A. Lail, M. B. Raschke, and G. D. Boreman, "Near-field measurement of infrared coplanar strip transmission line attenuation and propagation constants," Optics Express **18**(21), 21,678 (2010).

[50] H. C. Kim and X. Cheng, "Infrared dipole antenna enhanced by surface phonon polaritons," Optics Letters **35**(22), 3748 (2010).

[51] R. L. Olmon, M. Rang, P. M. Krenz, B. A. Lail, L. V. Saraf, G. D. Boreman, and M. B. Raschke, "Determination of electric-field, magnetic-field, and electric-current distributions of infrared optical antennas: A near-field optical vector network analyzer," Physical Review Letters **105**(16), 1–4 (2010). arXiv:1005.5567v1.

[52] T. Mandviwala, B. Lail, and G. Boreman, "Infrared-frequency coplanar striplines: Design, fabrication, and measurements," Microwave and Optical Technology Letters **47**(1), 17–20 (2005).

[53] F. Benson, "Waveguide attenuation and its correlation with surface roughness," Proceedings of the IEE - Part III: Radio and Communication Engineering **100**(64), 85–90 (1953).

[54] G. Gold and K. Helmreich, "Surface impedance concept for modeling conductor roughness," in *2015 IEEE MTT-S International Microwave Symposium*, vol. 0, pp. 1–4 (IEEE, 2015).

APPENDIX A: s-SNOM IN PSEUDOHETERODYNE DETECTION

A difficulty the s-SNOM has is the presence of large elastic scattering background that originates from the tip shaft of the probe and the sample [34]. Higher harmonic demodulation alone is insufficient to completely eliminate the background portion because a sensor responds to the intensity, which is quadratic in the field. To analyze how the background impacts the detected field and how to remove it, consider the scattered field phasor E_s as a Fourier series expansion

$$E_s = \sum_n \tau_n e^{in\Omega t},$$

where Ω is the tip vibration frequency. This field is a superposition of the near field E and the background field E_b, fields that can be written as Fourier expansion as well. Then the expansion coefficients $\tau_n = \sigma_n + \sigma_{b,n}$, where σ_n and $\sigma_{b,n}$ are the expansion coefficients of E and E_b.

At the detector, the scattered field produced a voltage u proportional to the intensity $I \propto |E_s|^2$. So the expansion coefficients for the voltage are given by

$$u_n = \kappa \sum_{j>n} \tau_{j-n}\tau_j^* + \tau_{j-n}\tau_j^* \approx \kappa(\tau_0\tau_n^* + \tau_0\tau_n^*),$$

where κ is a proportionality constant for the detector. The approximation is valid since $\tau_0 \gg \tau_{n>0}$. Additionally, the dominating coefficient $\tau_0 \approx \sigma_{b,0}$, therefore the voltage coefficient

$$u_n = \kappa[\sigma_{b,0}(\sigma_n^* + \sigma_{b,0}^*) + \sigma_{b,0}^*(\sigma_n + \sigma_{b,0})].$$

When higher harmonic demodulation is applied, background term $\sigma_{b,0}$ can be neglected compared with σ_n. So the term u_n can be approximated to

$$u_n \approx \kappa(\sigma_{b,0}\sigma_n^* + \sigma_{b,0}^*\sigma_n) = 2\kappa s_{b,0}s_n \cos(\varphi_{b,0} - \varphi_n),$$

where $\sigma_n = s_n e^{i\varphi_n}$ and $\sigma_{b,n} = s_{b,n} e^{i\varphi_{b,n}}$. As seen, the background term $s_{b,0}$ is still present at the n-th harmonic of the measured voltage. To fully eliminate this background term, s-SNOM can be operated in pseudoheterodyne mode.

Under pseudoheterodyne, the reference wave of the interferometer is modulated with a sinusoidal phase using a piezoelectric actuator. Therefore the detector output is proportional to a superposition of the scattered and the reference fields. The electric field phasor for the reference field can be written as

$$E_R = \rho e^{i[\gamma \sin(Mt) + \psi_R]},$$

where γ is the modulation depth for the reference mirror, M is the modulation frequency and ψ_R accounts for the average optical path difference between the signal and reference beam. By expanding this field in Fourier series

$$E_R = \sum_m \rho_m e^{imMt},$$

where the expansion coefficient is given by

$$\rho_m = \rho J_m(\gamma) e^{i(\psi_R + m\pi/2)},$$

and J_m is the Bessel function of the first kind and m-th order.

When the reference modulation M is smaller than the tip vibration frequency Ω, each scattered signal harmonic with frequency $f_n = n\Omega$ splits into sidebands with frequencies $f_{n,m} = n\Omega + mM$. The advantage of this modulation is that despite the background contributions are still superimposed at the harmonic frequencies $f_{n,0}$, at the sideband frequencies $f_{n,m\neq0}$. So the signal amplitude, with demodulation at

frequency $f_{n\neq0,m\neq0}$, $u_{m,n}$ = at the detector is given by

$$
\begin{aligned}
u_{n,m} &= \kappa(\tau_n \rho_m^* + \tau_n^* \rho_m) \\
&= 2\kappa\rho J_m(\gamma)s_{s,n}\cos(\varphi_{s,n} - \psi_R - m\pi/2).
\end{aligned}
$$

In the experiment, two signals at different demodulations are collected. Both signals are collected from the n-th harmonic, but the signals belongs to the second $m = 2$ and the first $m = 1$ sidebands, i.e., $u_{n,2}$ and $u_{n,1}$ respectively. Considering the addition of these two signals as

$$
\begin{aligned}
\frac{u_{n,2}}{J_2(\gamma)} + i\frac{u_{n,1}}{J_1(\gamma)} &= \kappa\left(\frac{\tau_n \rho_2^* + \tau_n^* \rho_2}{J_2(\gamma)} + \frac{\tau_n \rho_1^* + \tau_n^* \rho_1}{J_1(\gamma)}\right) \\
&= \kappa\left[\tau_n\left(\frac{\rho_2^*}{J_2(\gamma)} + i\frac{\rho_1^*}{J_1(\gamma)}\right) + \tau_n^*\left(\frac{\rho_2}{J_2(\gamma)} + i\frac{\rho_1}{J_1(\gamma)}\right)\right] \\
&= \kappa\left[\tau_n\left(\frac{\rho J_2(\gamma)e^{-i(\psi_R+2\pi/2)}}{J_2(\gamma)} + i\frac{\rho J_1(\gamma)e^{-i(\psi_R+\pi/2)}}{J_1(\gamma)}\right)\right. \\
&\quad \left. +\tau_n^*\left(\frac{\rho J_2(\gamma)e^{i(\psi_R+2\pi/2)}}{J_2(\gamma)} + i\frac{\rho J_1(\gamma)e^{i(\psi_R+\pi/2)}}{J_1(\gamma)}\right)\right] \\
&= \kappa\left[\tau_n\left(\rho e^{-i(\psi_R+2\pi/2)} + i\rho e^{-i(\psi_R+\pi/2)}\right) + \tau_n^*\left(\rho e^{i(\psi_R+2\pi/2)} + i\rho e^{i(\psi_R+\pi/2)}\right)\right] \\
&= \kappa\tau_n\rho e^{-i\psi_R}\left(e^{-i\pi} + ie^{-i\pi/2}\right) + \kappa\tau_n^*\rho e^{i\psi_R}\left(e^{i\pi} + ie^{i\pi/2}\right) \\
&= -2\kappa\tau_n^*\rho e^{i\psi_R}.
\end{aligned}
$$

Therefore

$$
\tau_n^* = -\frac{e^{-i\psi_R}}{2\kappa\rho}\left(\frac{u_{n,2}}{J_2(\gamma)} + i\frac{u_{n,1}}{J_1(\gamma)}\right),
$$

so the expansion coefficients for the scattered field is given by

$$
\tau_n = -\frac{e^{i\psi_R}}{2\kappa\rho}\left(\frac{u_{n,2}}{J_2(\gamma)} - i\frac{u_{n,1}}{J_1(\gamma)}\right).
$$

This expression can be simplified by choosing the appropriate modulation depth γ. Fig. A.1 shows the Bessel functions of the first kind and first and second order. For

$\gamma = 2.63$ the Bessel functions are equal $J_2 = J_1 = 0.462$. Then the coefficient is

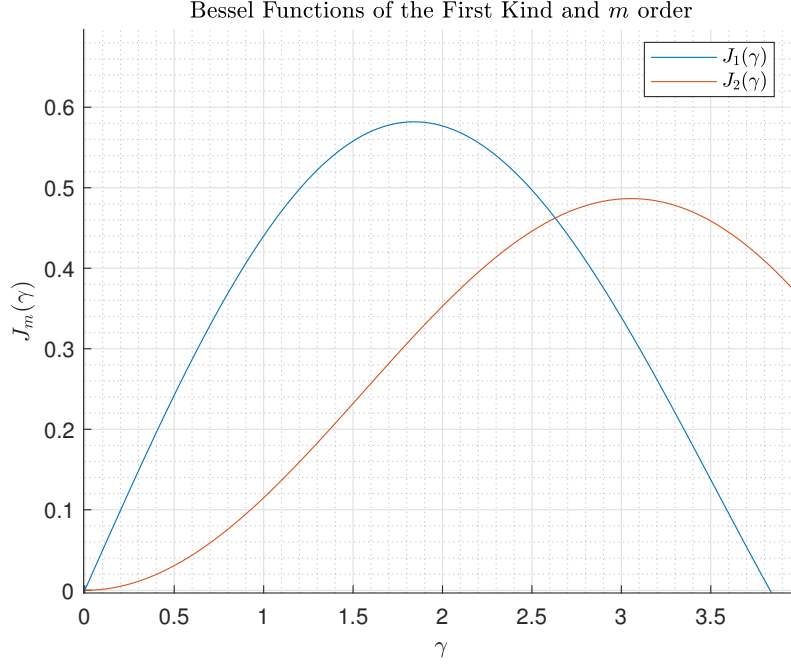$$\tau_n = \frac{2.16 e^{i\psi_R - \pi}}{2\kappa\rho}(u_{n,2} - iu_{n,1}). \tag{A.1}$$

Figure A.1: Bessel functions of the first kind.

Choosing the harmonic n, the coefficient τ_n measures the pure near field scattering since $\tau_n \approx \sigma_n$ [34]. Then, the near field amplitude s_n can be obtained as the modulus of τ_n, and the phase φ_n can be obtained from the argument of τ_n. Equation A.1 is the same as Eq. 3.10 used in the calculation of the near field and phase from the s-SNOM scans analyzed in this dissertation.

APPENDIX B: WIRE BONDING DETAILS

This appendix describes more in detail the procedure to obtain a successful wire bond between the chip carrier and the pads of the antennas described in Chapter 5.

Wire bonding was done with the WestBond Manual Wedge Bonder (Model 7476D) machine. The wire bonding machine possess a tip with a hollow channel. Through this channel a gold wire passes from a feed to a position underneath the tip. The bond is created when pressure from the tip and ultrasonic power is applied to the wire. This is a delicate process, but after several trials a procedure that worked on the wirebonding is described below:

- for a first bond: as depicted in Figure B.1, First make sure that there is enough wire in the tool tip to make the bond. Next, slowly bring the tool down until it makes contact with the sample. Once the bond is made, lift the tool up slowly. To obtain good results, lift the tool in a 45°direction with respect to the surface, this prevents the wire to break.

- for the second bond: as depicted in Figure B.2, very slowly bring the tool down until it makes contact with the pad, then make the bond. Once is done, slowly bring the tool up in a 45°direction, this will make the wire to break after the bond but without breaking the wire-pad bond.
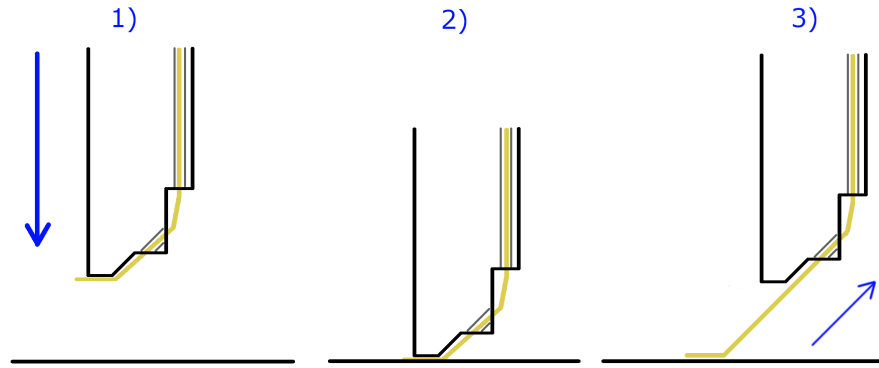
Figure B.1: Steps to make the first bond: 1) slowly bring the tool down until it reaches the sample. 2) gently let the tool make the bond and then lift the tool slowly. 3) lift the tool in a 45°direction towards the region of the second bond.
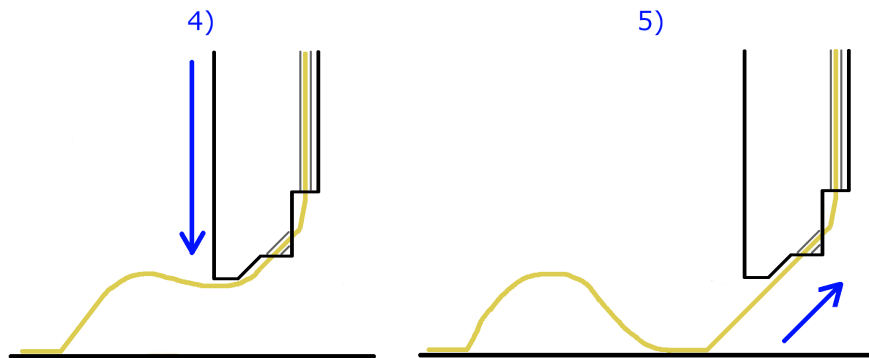

Figure B.2: Steps to make the second bond: 4) slowly bring the tool down until it reaches the sample and gently let the tool make the bond. 5) lift the tool up slowly in a 45°direction towards until the wire breaks.

The full machine parameters used for the wire bonding are described in Table B.1.

Table B.1: Machine parameters to wire bond antenna-coupled diodes to chip carrier.

Setting	Parameter
Bonds per wire	2
Ultrasonic power: Bond 1/2	300
Ultrasonic power: Bond 2/2	150
Ultrasonic time: Bond 1/2	300
Ultrasonic time: Bond 2/2	150
Loop height; mils, before bond 2/2	30 (762μm)
Machine setup: wire pull, motor steps	4
Machine setup: wire tail, motor steps	50
Machine setup: dual force	OFF
Machine setup: calibrate force	use force gauge...
Machine setup: beep upon contact	ON
Machine setup: must lift	ON

Additional actions to perform and to pay attention during wire bonding include

- For the first bond make sure there is enough wire on the end of the tool (use reflection of the tool on the wafer to see it from below). Then place the tool on top of a connector on the chip carrier. Slowly make the bond and slowly lift the tool from the surface to prevent the wire to break.

- Move the sample so the tool is now on top of the diode pad.

- Slowly make the bond on the pad by putting the tool down into the pad. Before lifting the tool, move it downward a bit and then lift up diagonally. This lift has to be done slowly to prevent damage/peeling on the pad.

The piece of silicon wafer in which the antennas are fabricated has to be well secured to the chip holder. This one had a piece of tape that did not hold well the wafer, so

when the tool was applying pressure, the sample wabble arround. This made difficult the wire bonding on the sample, leading to a couple of wires that did not stick to the pad. But after patiently and slowly making the bonds and allowing the wire to break gently, bonds were done on all the pads needed.

B.1 Troubleshooting

One of the most frequent problems that arise when wire bonding is the unthread of the wire from the tool. The threading of the wire is a delicate process. In order to make this easier, some steps that worked are described below

- In the machine console press the OPEN switch. This opens the clamps on the wire so it can be pulled without breaking.

- With a tweezers grab the end of the wire coming out form the tool and pull it downwards

- The pulled wire comes out straight. While grabbing the end of the wire, use the end of the tool to bend the wire in the shape it will go once threaded.

- With the tweezers, grab the bent wire and very carefully push it towards the hole in the tool to thread it. This might take a couple of times to get it right.

- Once the wire passes through the tool and some part of the wire is at the other end of the hole, pull the wire so it passes completely through the hole.

- In the machine console press the FEED switch so the clamps close and secure the wire. The machine is ready to make bonds now.

APPENDIX C: SUPPLEMENTAL EXPERIMENTAL DATA

C.1   Modified Folded Dipole

In the s-SNOM setup, the wafer that has the antennas is placed at the sample holder in the AFM. This holder is at a stage supported by three screws controlled by motorized micropositioners that adjust the height of the sample to engage or withdraw the sample when taking AFM scans. When conducting the experiments for the modified folded dipoles and t-match antennas, the motorized micropositioners in the AFM presented malfunctions that made the three screws turn at different speeds, therefore when adjusting the height with the motors, the sample holder is not horizontal. To correct this tilt in the sample, the motors were activated independently to compensate for the tilt and gauge blocks were used as a reference height to set all the motors. With this approach, the tilt was decreased as most as possible. However the engaging procedure of the AFM tip into the sample is entirely done by the motors, so there will be a tilt after the engaging is completed.
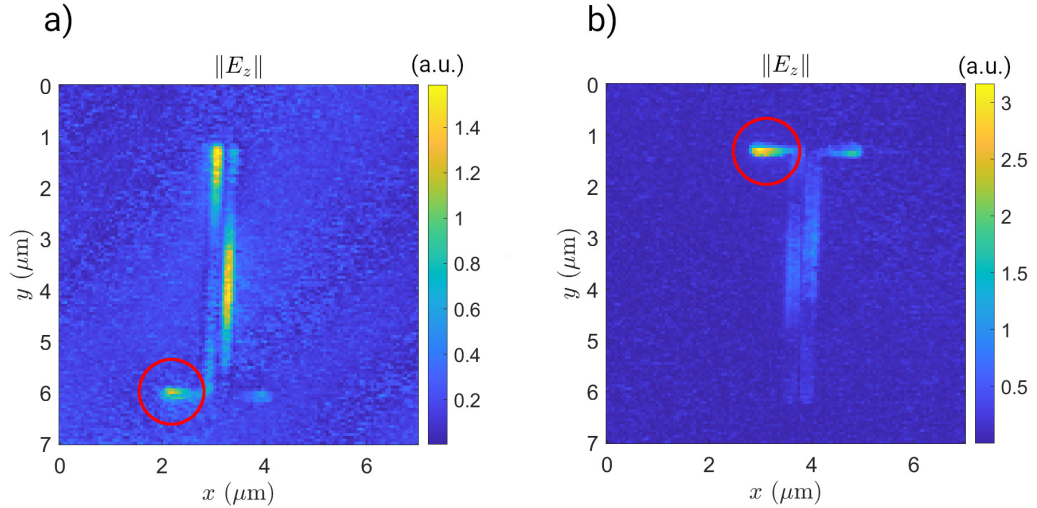

Figure C.1: a) s-SNOM scan for the open-circuit structure with the dipole oriented at the bottom of the frame. b) same structure as in a) but the sample was rotated 180°.

As a result of the tilt, some sections of the antenna would be closer to the tip

than others. Since the near-field enhancement is inversely proportional to the tip-antenna separation, then the measured near field at the antenna will be greater at those regions closer to the tip. To test this hypothesis two near-field measurements performed: the first one with the antenna with the same orientation as the antennas in Chapter 5, and the second one the antenna was turned 180° in the xy plane. The results are shown in Fig. C.1, where circled in red are the dipole arms at the left side of the frame. These arms have a higher near-field magnitude than the arm in the right side of the frame, which implies that the sample tilt causes the left side of the antenna to be closer to the tip than the right side.